

Copyright © 1973, by the author(s).
All rights reserved.

Permission to make digital or hard copies of all or part of this work for personal or classroom use is granted without fee provided that copies are not made or distributed for profit or commercial advantage and that copies bear this notice and the full citation on the first page. To copy otherwise, to republish, to post on servers or to redistribute to lists, requires prior specific permission.

PLASMA CONFINEMENT IN MULTIPLE MIRROR SYSTEMS II:
EXPERIMENT AND REACTOR CALCULATION

by

B. Grant Logan, I. G. Brown,
A. J. Lichtenberg, and M. A. Lieberman

Memorandum No. ERL-M387

1 March 1973

Electronics Research Laboratory

College of Engineering
University of California, Berkeley
94720

PLASMA CONFINEMENT IN MULTIPLE MIRROR SYSTEMS II:

EXPERIMENT AND REACTOR CALCULATION

B. Grant Logan, I. G. Brown,
A. J. Lichtenberg, and M. A. Lieberman

Department of Electrical Engineering
and Computer Sciences,
and Electronics Research Laboratory
University of California,
Berkeley, California 94720

ABSTRACT

A multiple mirror experiment confirms the predictions of theory that the axial confinement time exceeds that of a single mirror of the same length, and that the confinement scales as L^2 where L is the system length. The experiment indicates that the improved confinement occurs in an intermediate mean free path (mfp) regime in which the mfp for scattering out of a loss cone is of the order of a cell length. The absolute value of the axial confinement is smaller than the optimum confinement predicted from the theory by a factor between two and three, which is accounted for by the deviation of experimental parameters from optimum conditions. The scaling of the confinement time with mirror ratio is also investigated. A reactor calculation using the multiple mirror confinement time gives $Q_E = 2$ for a 400 meter system with 3000 MW(e) output.

* Work supported by National Science Foundation Grant NSF-GK-27538 and the Air Force Office of Scientific Research Grant No. AFOSR-69-1754.

PLASMA CONFINEMENT IN MULTIPLE MIRROR SYSTEMS II:

EXPERIMENT AND REACTOR CALCULATION

B. Grant Logan, I. G. Brown,
A. J. Lichtenberg, and M. A. Lieberman

I. INTRODUCTION

The theory of multiple mirror plasma confinement is presented in a companion article in this publication,¹ hereafter referred to as I. Experimental results on steady-state plasma confinement in a multiple-mirror device are the primary subject of this article. Preliminary experimental results with a simplified interpretation have been previously reported.² A more detailed analysis of the preliminary data and additional data will be given in Section III. Comparison with theory will also be presented in Section III. A reactor calculation based on the results of theory and experiment will be presented in Section IV. The present status of the multiple mirror concept will be summarized in Section V.

II. APPARATUS

The Berkeley Multiple Mirror Device (Fig. 1) consists of a series of water-cooled coils forming up to 8 mirror cells along a 6 cm. dia. 150 cm long vacuum chamber. A "Q" machine-type source produces a steady state alkali-metal plasma of variable mean free path (mfp) at one end to simulate ion confinement in a symmetric system which would have twice the number of mirror cells. Ions are created in the first mirror throat by contact ionization of lithium or potassium vapor on a hot tungsten plate (2 cm dia.), which also provides electrons by thermionic emission. In practice, the hot plate was not a perfect reflector

of ions due to surface recombination, as discussed in Appendix A. However, with potassium and operation with a negative plasma potential with respect to the hot plate (electron-rich operation), the surface recombination rate could be made small compared to the ionization rate of neutrals. Because of the high recombination probabilities for lithium, surface recombination was much more severe than with potassium, so most experiments were done with potassium.

The plasma length, which we designate as L' where L' is 1/2 of a symmetric system, was varied by moving a negatively biased collector plate along the chamber axis, as shown in Fig. 1. The end loss rate of ions was measured by the collector current I_c . The number of mirror cells $K = L'/\ell_c$ was varied either by moving the collector within a fixed multiple-mirror field, or by switching mirrors on and off between the source and a fixed collector. The plasma density was measured by a single Langmuir probe which could be moved both radially and longitudinally to explore the entire plasma volume.

With certain density and magnetic field parameters, large amplitude ($\delta n/n \sim 100\%$), nonsinusoidal fluctuations were observed on both the Langmuir probe current I_p and the collector current I_c . Within proper parameter regimes, however, the fluctuation levels were small ($\delta n/n \lesssim 1\%$). All longitudinal confinement experiments were conducted in stable regimes with low fluctuation level. However, radial loss persisted at low fluctuation level, as evidenced by the collector current I_c which decreased with increasing distance of the collector from the source faster than could be accounted for by surface recombination loss.

Such radial losses could result from DC convective drifts due to azimuthal temperature inhomogeneities on the hot plate. A method of subtracting out radial loss to obtain longitudinal confinement times is presented in the next Section.

The chamber was evacuated to less than 5×10^{-6} torr during experiments, so that ion-neutral collisions were always negligible compared to ion-ion collisions. Volume recombination was negligible at the typical ion densities ($n \sim 10^{10} \text{ cm}^{-3}$) in the experiment.

III. EXPERIMENTAL RESULTS

In I an axial containment time was derived which we shall use to compare with the experimental results. The confinement time against all losses may be defined, operationally, by the total number of ions within the system divided by the input flux SA_0

$$\tau_t = \frac{\int_0^{L'} n(z) A(z) dz}{SA_0} \quad (1)$$

where n and A are the plasma density and area respectively, and A_0 is the cross sectioned area of the mirror throat at which the flux density S is generated. An approximation to (1) gives

$$\tau_t = \frac{n_{\text{Ave}} \bar{A} L'}{SA_0} = \frac{n_{\text{Ave}} \bar{M} L'}{S} \quad (2)$$

where n_{Ave} , \bar{A} , and \bar{M} are separate averages over L' . We see that τ_t varies

approximately as the average mirror ratio,

$$\bar{M} = \frac{B_{\max}}{L'} \int_0^{L'} \frac{dz}{B(z)} \quad (3)$$

and thus we shall use this averaged quantity in describing the experimental results (we note that \bar{M} is somewhat different from the M_{eff} used to describe the one dimensional containment, the difference arising from the three dimensional nature of the flux lines).

A. Confinement time with 5 cells

The magnetic field for most confinement experiments consisted of 5 identical mirror cells each with an average mirror ratio $\bar{M} = 2.2$ (peak $M = 3.7$). Figure 2 shows typical probe currents as a function of probe position in (a) low, (b) intermediate, and (c) high density regimes, measured by the Langmuir probe centered on the axis and moved from the source at $z = 0$ to the collector at $z = 140$ cm. The ion-ion mfp λ , estimated from ion temperature calculations in Appendix B, is indicated for the middle cell in each density regime. In the low density regime Fig. 2a, a nearly uniform density at corresponding points in all cells is found, with a modulation due to the mirrors as expected for a collisionless beam. The midplane densities are not a factor of M less than in the throats, indicating some trapped particles in each cell. Because the mfp $\lambda \gg L'$, however, little multiple-mirror retrapping is expected. At intermediate densities (Fig. 2b), a steep density gradient is observed, the density dropping nearly linearly from cell to cell from the source, indicating impedance to free flow by the mirrors. The mfp for scattering into an average loss cone angle ($\lambda^* \approx \lambda/\bar{M}$) is about one cell

length $\ell_c = 28$ cm at the average density. At higher densities (Fig. 2c), a more uniform density from cell to cell is observed, characteristic of MHD flow¹.

Figs. 3a, b and c show the collector current as a function of collector position corresponding to the density profiles of Fig. 2a,b, and c, respectively. Fig. 3 indicates little or no radial loss for the low density regime (a), and a moderate rate of radial loss for the intermediate (b) and high density (c) cases. In Figs. 3a, b, and c there is an anomalous change in collector current when the collector passes the second mirror at $z = 28$ cm which does not follow the subsequent behavior of the collector current with increasing z . Also in Fig. 3 (b) and (c), there is a modulation of I_c with the cell length, I_c being higher in the midplanes than in the mirror throats. These effects may be due to instrumental effects or due to real changes in radial loss rates with collector position. In each of (a), (b) and (c), the highest value of I_c occurring over an interval of a cell length is taken as the measure of the end loss flux, and the highest value occurring in the first cell $\left[\equiv I_c(0) \right]$ is taken as a measure of the source strength SA_0 .

From Eq. (1), the total containment time, including radial loss, is given by

$$\tau_t = \frac{q \int_0^{L'} n(z) A(z) dz}{I_c(0)}, \quad (4)$$

where q is the ion charge and $A(z)$ is the effective plasma cross section at the density $n(z)$. The density $n(z)$ is an average over the radius at point z . Typical radial density profiles, taken at 4 consecutive mirror

throats, are shown in Fig. 4 for (a) low, (b) intermediate, and (c) high density regimes. In Fig. 4. r_c is the collector radius, r_o is the hot plate radius, and $r_a = r_a(0)[B(0)/B(z)]^{1/2}$ is an aperture radius set by a heat shield in front of the hotplate, and projected along the field lines. The top radius scale in Fig. 4 is contracted by a factor of \sqrt{M} from the bottom scale to show the relative plasma size in the mid-planes. In a previous report,² the simplest estimate for $A(z)$ in Eq. (1) was made by integrating the entire radial profiles out to the wall radius, resulting in optimistic values of τ_t . In this analysis, however, plasma at radii beyond $r_a(z)$ will be considered lost radially and we therefore take $A(z) = \pi r_a^2(z)$. The appropriate density $n(z)$ is then

$$n(z) = \frac{1}{A(z)} \int_0^{r_a(z)} n(z,r) 2 r \pi dr.$$

Note that if we measure I_c near a midplane, $r_a(z) \approx r_c$ from Fig. 4.

Since the total source flux $SA(0) \approx I_c(0)/q$ divides into surface recombination loss, radial loss, and end loss to the collector when the collector is at $z = L'$, τ_t by Eq. (4) includes all types of loss. The confinement time against end loss to the collector, alone, is defined

by

$$\tau_z \equiv \frac{q \int_0^L n(z) A(z) dz}{I_c(L')} \quad (5)$$

However, because of the effect of a distributed radial loss on the density profile $n(z)$, τ_z given by Eq. (5) with $I_c(L') < I_c(0)$ is theoretically larger than $\tau_t = \tau_z$ with no radial loss [$I_c(0) = I_c(L')$]. Thus, to compare with theoretical values of τ_{mm} which do not include radial loss,

we calculate a factor ζ , in Appendix C, such that $\tau_{\text{mm}}(\text{exp}) = \zeta \tau_z(\text{exp})$.

Using probe and collector current profiles such as in Figs. 2 and 3, and using Eq. (1), (4), and (5), values of τ_t , τ_z and τ_{mm} normalized to an ion transit time L'/\bar{v} , denoted by τ_t^0 , τ_z^0 and τ_{mm}^0 , respectively, are plotted as a function of average density $n_{\text{Ave}} = (1/L') \int_0^{L'} n(z) dz$ in Figs. 5 and 6. The τ 's are normalized to $L'/2\bar{v}$ so that they are independent of $\bar{v}(\tau - n - I_p/q\bar{v})$ and thus ion temperature T_i which could not be easily measured and for which calculations are somewhat involved (see Appendix B). Fig. 5 shows data exhibiting a relatively low rate of radial loss, and Fig. 6 shows data with a relatively higher rate of radial loss, which is thought to be the result of changes in the heat shields and alignment of the source from that of Fig. 5, or possibly the result of the slightly higher mirror ratio used in Fig. 6. In both Fig. 5 and Fig. 6, τ_{mm}^0 approaches 1 at densities below 10^9 cm^{-3} as expected when collision rates are low, and increases with density to a maximum of about 8 near $n_{\text{Ave}} = 10^{10} \text{ cm}^{-3}$ at which the mfp for scattering into an average loss cone angle $\bar{\lambda}/\bar{M} \approx \ell_c$. The peak of τ_{mm}^0 occurs at a slightly higher average density in Fig. 6, presumably due to the higher rate of radial loss. As the average density is increased further, τ_{mm}^0 decreases as would be expected for onset of MHD flow.¹ At $n_{\text{Ave}} = 5 \times 10^{10} \text{ cm}^{-3}$ ($n_1 \approx 8 \times 10^{10}$ at the source), $\lambda \approx 6 \text{ cm}$ from Appendix B, which is approximately equal to the mirror width $B(\text{dB}/dz)^{-1}$ (See Fig. 10). At $\bar{n}_{\text{Ave}} \sim 1.5 \times 10^{11} \text{ cm}^{-3}$, $\lambda \sim 1 \text{ cm}$ approaches the average potassium ion cyclotron orbit $2\pi\bar{\rho}_i$, at which Larmor motion and conservation of ion magnetic moment is destroyed. Thus the decrease in τ_{mm}^0 in Figs. 5 and 6 at the higher densities is consistent with onset of MHD flow. In the MHD limit, τ_{mm}^0 would be approximately the value \bar{M}^{-1} .

B. Scaling with number of mirror cells.

One test of the scaling law of multiple mirror confinement time with the number of mirror cells can be made by observing the changes in the density in the first cell, n_1 , for a constant source, as the collector is withdrawn within a fixed multiple mirror field, thus adding mirror cells to the system. Fig. 7 shows the probe current (\propto density) in the first cell next to the source as a function of collector position in the (a) low, (b) intermediate, and (c) high density regimes. The experimental conditions for Fig. 7 were the same as for Figs. 2 and 3. In Fig. 7 the density at the source is seen to increase in a stepwise fashion as the collector passes each mirror throat, adding another cell to the system. The increase in density is strongest in the intermediate density regime, as expected. The first density jump corresponding to the collector passing the second mirror is a result of partial filling of velocity space due to ion trapping when the first cell is created. It is not a multiple-mirror effect, and only jumps following the first are used as a measure of improvement in confinement with multiple-mirrors over the confinement with one mirror cell. The ratio of n_1 with 5 mirror cells (n_{\max}) to n_1 with one mirror cell (n_{\min}) is plotted as a function of $\frac{1}{2} n_{\max}$ ($\frac{1}{2} n_{\max} \approx n_{\text{Ave}}$ in the intermediate density regime) in Fig. 8. The τ_{mm}^0 curve from Fig. 5 is also shown for comparison. The values of n_{\max}/n_{\min} are seen to generally follow the values of τ_{mm}^0 .

Although the density in cells other than the first were not measured for collector positions other than $z = L'$, the density profiles with the collector at $z = L'$ such as Fig. 2 can be used to estimate n_{Ave} in terms of n_1 in the various density regimes, for $K = 5$ cells. In

the short and long mfp regimes of Fig. 2a and 2c for example, the axial profile is roughly uniform and $n_{\text{Ave}} \approx n_1$, while for Fig. 2b, $n_{\text{Ave}} \approx \frac{1}{2} n_1$. Assuming the same ratios of n_{Ave}/n_1 for any number of cells $2 < K \leq 5$ in the same mfp regime, the average density $n_{\text{Ave}}(K)$ can be estimated from the values of $n_1(K)$ in Fig. 7 for each collector position corresponding to K cells. Neglecting correction factors for radial loss effects on the density profile, the longitudinal containment time for K cells $\tau_z(K)$ be taken proportional to

$$\tau_z(K) \sim n_{\text{Ave}}(K) (L') / I_c (L') \quad , \quad (6)$$

where $L' = K\ell_c$ is varied by increments of ℓ_c . Taking $n_{\text{Ave}}(K) \approx \frac{1}{2} n_1(K)$ from Fig. 7, and using Fig. 3 for $I_c(L')$, the resulting values of τ_z for 1 to 5 cells, in arbitrary units normalized to the τ_z obtained with $K = 1$, are presented in Table A below along with the theoretical ratio

$$\frac{\tau_{\text{mm}}(K)}{\tau_{\text{mm}}(1)} = \frac{1}{\Delta n} \sum_{j=1}^K n_j \quad , \quad (7)$$

Where Eq. 28 of Ref. (1) is used for n_j .

Table A

Experimental and Theoretical Scaling of Containment Time
with Number of Cells K, Normalized to $K = 1$

K	$\tau_z(K)$ (Experiment)	$\tau_{\text{mm}}(K)$ (Theory)
1	1	1
2	3.4	3
3	6.2	6
4	10.6	10
5	16.4	15

The values of $\tau_z(K)$ for $K > 1$ in Table A are somewhat larger than theory, because $\tau_{mm}(th)$ is compared with $\tau_z(exp)$ rather than with $\tau_{mm}(exp)$ which cannot be calculated in this case. Nonetheless, the agreement between theory and experiment on the scaling of τ_{mm} with L must be considered good for the uncertainties involved in the comparison. Note that while the increases in n_1 in Fig. 7 become smaller for $K = 4$ and 5 due primarily to increasing radial loss relative to end loss, $\tau_z(K)$ continues to increase approximately as L^2 (or K^2) due to the decrease in I_c with K , as seen in Fig. 3.

Another test of the scaling of confinement time with the number of mirror cells K can be made by observing the changes in density with increasing K with L' constant, by switching on additional mirrors between a constant source and a fixed collector at $z = L'$. The density with 3 cells was compared to the density with 1 cell (called a long mirror cell) for the same total length L' and source strength S . The magnetic field profiles for these two cases are shown in Fig. 9.

Figure 10 shows density profiles in the low density regime for 3 cells and 1 cell (long mirror). The density follows the field variation of Fig. 9 closely in each case, indicating collisionless behavior. Fig. 11 shows the density profiles in the intermediate density regime. The density with multiple mirrors is everywhere higher than with only 1 cell, indicating considerably improved confinement. The multiple-mirror density profile shows the characteristic stair-step shape predicted from theory.¹ The midplane density is approximately the density in the mirror throats, as expected for a plasma that is locally Maxwellian at all points. To quantify the comparison in terms of confinement time $\tau \sim \bar{n}_{Ave}$, the

the ratio of average midplane densities (we use a bar, here, for the spatial averages)

$$\frac{\bar{n}_{mm}}{\bar{n}_{\ell m}} = \frac{\frac{1}{3} \sum_{j=1}^3 n_j^{(mm)}}{n(\ell m)} \quad (8)$$

can be considered, which is the ratio of confinement times if the mirror width and changes in plasma volume due to the finite mirror width are neglected. In Eq. (8), n_{mm} and $n_{\ell m}$ denote the densities with the 3 cell multiple-mirror field and the long mirror field, respectively. The results for $\bar{n}_{mm}/\bar{n}_{\ell m}$ taken from curves such as in Figs. 10 and 11 are plotted in Fig. 12 as a function of twice the long mirror midplane density $2 n_{\ell m}$, which is approximately the average multiple mirror density in the intermediate density regime. The ratio $\bar{n}_{mm}/\bar{n}_{\ell m}$ increases from 1 at low densities to the theoretical 3 cell maximum of 2 at higher densities. The ratio of 2 holds over a wider range of densities than the peak of τ_{mm}^0 such as in Figs. 5 and 6, possibly because both τ_{mm} and $\tau_{\ell m}$ can decrease to some extent from maximum values keeping nearly the same ratio. In the MHD limit, however, the ratio $\bar{n}_{mm}/\bar{n}_{\ell m}$ is expected to approach unity. The scatter of points about the solid line curve fit is due primarily to small drifts in the source strength between measurements of \bar{n}_{mm} and $\bar{n}_{\ell m}$.

C. Scaling of confinement with mirror ratio

To examine the dependence of multiple-mirror confinement on the mirror ratio M , the variation of n_{max}/n_{min} with M was measured rather than τ_{mm}^0 , since n_{max}/n_{min} was much easier to measure while still being related to confinement time as indicated in Fig. 8. Figure 13 shows a

family of n_{\max}/n_{\min} curves plotted as a function of n_{\max} , for five cells and numbered from 1 to 8 corresponding to 8 values of M and \bar{M} as given in Table B below:

Table B

Values of M and \bar{M} for Fig. 13

#	M	\bar{M}
1	1.45	1.40
2	2.55	2.01
3	3.27	2.20
4	3.70	2.31
5	4.51	2.82
6	5.72	3.13
7	6.50	3.39
8	12.0	5.26

The mirror ratios for all cells were the same.

The location of the peak values of n_{\max}/n_{\min} for increasing M or \bar{M} in Fig. 13 consistently decrease to lower values of n_{\max} with increasing mirror ratio. This is believed to correspond to the dependence of the mfp for scattering out of the loss core λ^* as $1/nM$. Thus a given value of λ^* , which optimizes trapping, can be achieved with lower densities at higher M values. We note that the peak values of n_{\max}/n_{\min} first increase and then decrease with increasing M . The magnitudes of the peak values of n_{\max}/n_{\min} are less than the maximum value of 5, due to the combined effects of average plasma drift, ambipolar effects, radial loss, and MHD effects. At $M = 3.27$ (curve number 3), the maximum

mirror and midplane fields were applied, limited by the generator power. To create higher mirror ratios, the midplane field was reduced, keeping B_{\max} the same. To make M smaller than 3.27, B_{\max} was reduced, keeping B_{\min} constant. Since changes in M from 3.27 reduced the average field strength, the degree of radial loss and MHD effects probably also changed. This is one reason for the magnitude of the n_{\max}/n_{\min} peaks to be optimized near the value of $M = 3.27$.

III. COMPARISON OF τ_{mm} EXPERIMENT WITH THEORY

The theory of multiple mirror confinement¹ was developed assuming sharp mirrors [$B(dB/dz)^{-1} \ll \ell_c$] for which $\bar{M} = M$. With mirror widths comparable to ℓ_c in the experiment, however, $\bar{M} < M$. If $\bar{M} = 2.2$ for all cells, corresponding to the conditions of the experiment in Figs. 5 and 6, then Eq. 29 in I, with $M = 2.2$, predicts a maximum containment time $\tau_{\text{mm}}(\text{max}) = 2MK (L'/\bar{v}) = 22(L'/\bar{v})$ for $K = 5$ cells, about a factor of 2.7 times larger than the maximum of $\tau_{\text{mm}}(\text{exp}) \approx 8 (L'/\bar{v})$ from Fig. 5 or Fig. 6.

The maximum experimental values are less than the maximum theoretical values for reasons other than the presence of radial and recombination losses in the experiment, which are already accounted for in $\tau_{\text{mm}}(\text{exp})$. The condition on the mfp, λ , that $B/(dB/dz) \ll \lambda \ll \ell_c$ for Eq. 29, in I is not satisfied in the experiment. With $\lambda^* \approx \lambda/\bar{M} \approx \ell_c$ in the experiment we find from Fig. 2 of I that the ratio of the diffusion coefficient to the minimum diffusion, $D/D_{\min} > 2$, and therefore gives a containment considerably less than maximum. Also, the condition that $\lambda \sim B(dB/dz)^{-1}$ in the experiment implies some loss of confinement due to MHD effects. The use of moderate mirror ratios and a small number of cells leads to

non-negligible drift velocities compared to the thermal velocity in the experiment (maximum $\tau_z^0 \sim 10$ in Figs. 5 and 6 suggest average longitudinal drift velocities $V_d \sim 0.1 \bar{v}$). This effect shortens the containment time to some degree, although the results of numerical computations, including drift velocity self consistently, (see Fig. (10) of Ref. 1) indicate that the effect is not large. Finally, it should be noted that ambipolar effects, in the experiment, are estimated to increase \bar{D} by a factor of about 1.5. Some of the difference between experimental theoretical values of τ_{mm} is due to the neglect of this factor in the theory.

One quantity, of some theoretical importance, that can be calculated approximately with the aid of the experimental data, is the ratio of the momentum transfer mean free path λ^* to the mean free path for scattering out of the loss cone λ/\bar{M} , i.e.,

$$\lambda^* = \alpha \lambda/\bar{M} \quad (9)$$

From the theory and numerical calculations of sections III and V of Ref. 1 we found $\alpha \approx 1$. Provided MHD and ambipolar effects can be taken into account, we can obtain an estimate of α by finding at what value of λ^* the ratio $\tau_{mm}/\tau_{mm}(\max)$ that we would expect from Fig. 2, Ref. 1 is equal to the value of $\tau_{mm}(\text{exp})/\tau_{mm}(\max)$ found experimentally. This value of λ^* can then be compared with the measured value of λ/\bar{M} to find α .

For example, using the density profile of Fig. 2b which has an $n_{\text{Ave}} = 6.10^9 \text{ cm}^{-3}$ this corresponds to a $\tau_{mm}^0(\text{exp}) = 6$ from Fig. 5. The theoretically maximum value of confinement time, for these parameters, is 22 giving a ratio

$$\tau_{mm}^0(\text{exp})/\tau_{mm}^0(\max) = .27$$

MHD effects are not apparent in Fig. 2b, and we neglect them. For simplicity we take $\tau_{\text{mm}}/\tau_{\text{mm}}(\text{max}) = \bar{D}_{\text{min}}/\bar{D}(\bar{n})$ i.e., we assume that the density is constant at the value \bar{n} , so that the confinement time is inversely proportioned to the diffusion coefficient. Since the experimental value of \bar{D} is 1.5 times the value it would have without ambipolar forces we use the value $\bar{D}_{\text{min}}/\bar{D}(n_{\text{Ave}}) = 0.27 (1.5) = 0.4$, to obtain the value of $\lambda^*/\ell_c \approx 0.5$ from Fig. 2, Ref. 1, as the experimental value for the momentum transfer mean free path. From Appendix B we estimate $\lambda(n_{\text{Ave}}) \approx 40$ cm and, with $\bar{M} = 2.2$ and with $\ell_c = 28$ cm, we obtain the experimental value $\lambda/\bar{M}\ell_c = .65$. From (9) we then have $\alpha = 0.78 \approx 1$, thus experimentally confirming our analytic and numerical results. It also permits us to use Fig. 2, Ref. 1, for calculating reactor parameters, which we do in the following section.

IV. REACTOR CALCULATION

A preliminary evaluation of the significance of the multiple mirror concept can be made by estimating parameters for a steady state reactor (assuming no anomalous radial loss). We have the following powers (watts) of energy flow associated with the length L of a DT multiple-mirror fusion reactor: Fusion neutron power produced in the blanket, including the $\text{Li}^6 (n,T) \text{He}^4$ reaction energy with a tritium breeding ratio of 1.5, (6)

$$P_n = 2 \int_0^{L/2} \frac{1}{4} n^2(z) \langle \sigma v \rangle (z) E_n A(z) dz, \quad (10)$$

where $E_n = 14.1 + 1.5 (4.8) = 21$ MeV is the energy per reaction deposited in the blanket, $\langle \sigma v \rangle$ is the reaction rate, and $A(z)$ is the effective plasma cross sectional area at density $n(z)$. Fusion α -particle power produced in the plasma,

$$P_{\alpha} = P_n (E_{\alpha}/E_n) \quad , \quad (11)$$

where $E_{\alpha} = 3.5$ MeV is the α -particle energy of the DT reaction.

Bremsstrahlung power loss,⁶

$$P_{\beta} = 2 \int_0^{L/2} 5 \times 10^{-37} n^2(z) T(z)^{1/2} A(z) dz, \quad (12)$$

(n in m⁻³, T in KeV).

Power loss associated with plasma loss along field lines,

$$P_{\ell} = 8[Q/kTF] kT(z) \bar{D}(z) \nabla n(z) A(z), \quad (13)$$

where we have written $P_{\ell} = 4Q(z) A(z)$ with Q the energy flux density,

with the factor of 4 taking into account loss through both ends and the

fact that electrons carry off an equal amount of energy as the ions.

The ratio $[Q/kTF]$ is taken from Fig. 2, Ref. 1, and the particle flux

density $F(z) = -2\bar{D}(z) \nabla n(z)$, with the factor of 2 to account for ambi-

polar diffusion. In the steady state $P_{\ell} = \text{const.}$ We take $B_{\text{max}} = \text{const.}$,

a practical magnetic field limit in all mirror throats. Then we adjust

$B(z)$ in the mirror midplane such that

$$\beta = [2n(z) kT(z)]/[B^2(z)/2 \mu_0] = \text{const.}, \quad (14)$$

which allows for the maximum mirror ratio in each cell at the maximum

allowable β . From conservation of flux

$$A(z) = A_0 M(z) \quad , \quad (15)$$

where A_0 is the area of the mirror throats.

From (14), assuming $T(z) \approx \text{const.}$

$$M(z) \approx M_1 [n_1/n(z)]^{1/2} \quad (16)$$

Assuming the cell length $\ell_c = \text{const.}$, from diffusion theory one then obtains, approximately,

$$n(z) \approx n_1 \left(1 - \frac{z}{\chi}\right)^{3/2} \quad (17)$$

$$T(z) \approx T_1 [n(z)/n_1]^{1/12} \quad (18)$$

where z measures the distance along the density gradient region of length χ (allowing $\chi < L/z$). Eq. 18 indicates that for practical purposes the variation of T with z can be neglected. The subscript 1 refers to values taken at the maximum density n_1 in the center of the reactor. In order to choose ℓ_c , Q must be chosen to be near its minimum value over the range of $\lambda^*(z)$ for the reactor, while at the same time using as few mirrors as possible, subject to the above constraint. Since $F \propto D$ and $D_{\min} \propto \ell_c$, we use Fig. 2, Ref. 1 to graphically compute

$$Q \propto \frac{Q D}{kTF D_{\min}} \ell_c$$

which is found to be quite flat in the range $.2 < \lambda^*/\ell_c < 4$, slowly decreasing for $\lambda^*/\ell_c > 4$, and slowly increasing for $\lambda^*/\ell_c < .25$. We therefore chose ℓ_c as large as possible consistent with this inflection region, taking $\lambda^*/\ell_c = .25$ at $n = n_1$, i.e.

$$\ell_c = 4 \lambda^* = 4 \lambda/M \quad (19)$$

We assume P_n and P_β is converted into electricity by a thermal cycle at efficiency η_T , P_α is deposited directly within the plasma, and P_ℓ is directly converted into electricity at efficiency η_{DC} . Taking the reinjection efficiency to be unity a power flow diagram is constructed as in Fig. 14. From Fig. 14, the following power ratio Q_E , defined as

$$Q_E \equiv \frac{P(\text{total electrical power generated})}{P(\text{injected, or recirculating electrical power})}$$

is calculated to be

$$Q_E = \frac{\eta_T [P_n + P_\beta + (1 - \eta_{DC})P_\ell] + \eta_{DC}P_\ell}{P_\ell + P_\beta - P_\alpha} \quad (20)$$

For $P_{net} \geq 0$, $Q_E \geq 1$. Using Eqs. 20 and 10 to 13 together with Eqs. 15-18, Q_E can be optimized with respect to the axial profile as given in Fig. 15 for fixed L , with the results also given in Fig. 15. In Fig. 15 the shape optimization does not yield a significant advantage in Q_E but indicates one can operate with $2 X/L = .5$ at the same $Q_E = 1$ of a triangular density profile, with substantially improved power distribution. Using this value of $2 X/L$, together with Eqs. 15-19, then Eqs. 10-13 can be integrated approximately to yield

$$P_n \approx \frac{1}{6} n_1^2 \langle \sigma v \rangle E_n A_1 L \quad (21)$$

$$P_\alpha \approx \frac{1}{6} n_1^2 \langle \sigma v \rangle E_\alpha A_1 L \quad (22)$$

$$P_\beta \approx 3.3 \times 10^{-37} n_1^2 T^{1/2} A_1 L \quad (23)$$

$$P_\ell \approx \frac{185 \text{ kT } \lambda_1 \bar{v} n_1 A_1}{M^2 L} \quad (24)$$

Eq. 20, together with Eqs. 21-24 can be used to minimize L with respect to T. Choosing a reasonable value of $Q_E = 2$ we obtain the results in Fig. 16, which indicate that operation near the ignition point with $T = 4.5$ KeV is best. For $Q_E = \infty$, corresponding to the self sustaining condition $P_\alpha = P_\ell + P_\beta$, a curve of L versus T similar to Fig. 16 indicates a minimum at $T = 6$ KeV.

The maximum density n_1 is set by limits on B_{\min} in the central region of the reactor, and by the plasma beta defined by Eq. 17. An upper limit on $B_{\min} = 200$ kG is assumed for superconducting magnets, and an upper limit on average beta of $\bar{\beta} = .8$ is taken. For this value of β a perpendicular diffusion coefficient $D_\perp = 10^{-3} D_{\text{Bohm}}$ can be tolerated.⁽⁴⁾ Peak mirror fields of $B_{\max} = 300$ kG can be provided by small conventional coils placed inside the blanket which add 100 kG to the superconducting field, consuming less than 10% of the power output. An internal mirror ratio $M = B_{\max}/B_{\min}$ (inside) ≈ 2.7 is then created at $n = n_1$.

Using $B_{\min} = 200$ kG, $B_{\max} = 300$ kG, and $\bar{\beta} = 0.8$, $\eta_T = .5$ and $\eta_{DC} = .75$ and substituting Eqs. (21-24) into Eq. (20), Q_E is plotted as a function of L in Fig. 17. The breakeven condition indicated in Fig. 17 at $L = 140$ meters is sensitive to the conversion efficiencies η_T and especially η_{DC} . However, Q_E is insensitive to η_T and η_{DC} for $Q_E > 2$, becoming completely independent of η_T and η_{DC} at the self sustaining condition at $L = 1100$ meters, where no injection of energy is required.

The minimum length for economic operation is probably $L = 400$ meters, which corresponds to $Q_E = 2$, or net electrical power output $P_{\text{net}} = P$

(recirculating). At that point the parameters of interest are $T_e = T_i = 4.5$ KeV, $n_1 = 8 \times 10^{16} \text{ cm}^{-3}$, $\lambda(n_1) = 3.3$ meters, $l_c = 5.0$ meters (20 cells on each side in the density gradient regions), $\tau_{\text{mm}} \approx 30$ millisecc. The minimum economic power output P_{net} is directly related to the length L or the central region of high field $L/2$. There is a minimum power output per unit length required to meet a given capital cost per kW(e) for a given cost $/\text{m}^2$ of superconducting coils with the constraint of a minimum blanket thickness of ≈ 1 meter. Using estimates of magnet costs (expected to be the most costly single item for superconductor fields $B > 100$ kG) from Rose⁵ and assuming a capital cost per net electrical kilowatt of $\$200/\text{kW(e)}$, the power output would need to be of the order of $10 \text{ MW(e)(net)}/\text{meter}$ in the central region of length $L/2$. Thus $P_{\text{net}} \approx 3000 \text{ MW(e)}$ total net power for $Q_E = 2$, a useful power level. A plasma diameter of 3 cm would be required to produce the 10 MW(e) net per meter at $T = 4.5 \text{ KeV}$.

For $Q_E = 2$, 3000 MW(e) of injected power would be required to sustain the reaction. If this power were injected by neutral beams at the characteristic energy of the plasma of 4.5 KeV , it would require $6.5 \cdot 10^5$ amperes of beam current; this appears to be a very severe requirement, particularly at the low 4.5 KeV energy. However, an alternative method exists in which the plasma current is supplied by pellet injection, as envisioned for toroidal devices, and the energy is supplied separately. Two methods of supplying the energy, that are in principle feasible today, are by high energy neutral injection transverse to the device, and by electron beam injection axially. The former, with injection at 150 KeV , would require $2 \cdot 10^4$ amperes of current, a requirement not very different

from that envisioned for a single mirror reactor. The latter method, with injection at 100 KeV, would require 3.10^4 amperes of electrons, steady state, a value that has already been exceeded in intense relativistic beams, for short pulses. It has been shown that, even in the absence of strong collective effects, a 100 KeV electron beam will collisionally transfer most of the energy along a plasma column of the density and length of the proposed reactor.⁷

The preceding calculation of reactor parameters is intended to serve as a comparison with other reactor configurations, rather than as a complete feasibility study. A number of possibilities exist for improving the system performance, which should be investigated in a more comprehensive study. A more general optimization of the magnitude and spacing of the magnetic mirrors, under various constraints, can be made. Preliminary calculations have indicated that improved total performance can be achieved by seeding the plasma with a small percentage of higher Z material, and by increasing the density near the system ends with colder plasma. Energetic neutral injection can also make a significant enhancement to Q_E (or system shortening) because of the initial confinement time, during which the energetic particles are degrading in energy.⁸ The possibility also exists for decoupling the mean free path from the density by introducing a non adiabatic component in the external field.⁹

V. SUMMARY AND CONCLUSIONS

The theory of multiple mirror confinement predicts that an intermediate mean free path (mfp) regime exists for which ions are lost axially from a multiple mirror system by a random walk process. This

implies a scaling of confinement time as $\tau_{\text{mm}} \propto L^2$ which is favorable for reactor design. The experimental determination of τ_{mm} under stable conditions indicates a confinement time a factor of 2 to 3 below the theoretically maximum confinement. This difference is accounted for primarily by the merging of the long and short mfp regimes, so that the full potentialities of the intermediate mfp regime cannot be realized in the experiment. The scaling to a reactor would produce a well defined intermediate mfp regime such that only ambipolar effects would reduce the axial confinement time below the theoretical maximum given in Eq. (29) of Ref. 1. On the basis of these results a reactor calculation indicates that the multiple mirror concept results in a reasonable power and size (a 400 meter reactor gives $Q_E = 2$ with 3000 MW(e) of useful output).

The multiple mirror experiment consisted of simple mirrors which would produce a hydromagnetically unstable plasma in a reactor configuration. In the experiment the plasma is stabilized by line-tying to the hot plate. The introduction of multipolar windings to achieve an average minimum B system does not substantially change either the axial confinement or the reactor economics. However, the stability of the average minimum B fields, with respect to localized modes, remains to be investigated. A program is now underway to do this. Since the loss cones are essentially full, in the multiple mirror configuration, there should be no difficulties with velocity space instabilities.

APPENDIX A. Surface Recombination Loss

The relative probabilities, or ratio of surface densities ψ_i and ψ_0 for ions and neutrals respectively, is given by the Langmuir-Saha equation

$$\frac{\psi_i}{\psi_0} = \left(\frac{\omega_i}{\omega_0} \right) \exp \left[-q (\phi_i - \phi_{wi}) / kT_s \right] \quad (1A)$$

where (ω_i/ω_0) is the ratio of statistical weights ($\omega_i/\omega_0 = 1/2$ for alkali metals), ϕ_i is the ionization potential of the alkali neutral, and ϕ_{wi} is the effective work function for ionization. (ϕ_{wi} is not always equal to the work function for electron emission ϕ_{we}). The ionization probability P for a neutral striking the hot plate is obtained from

$$P = \frac{1}{1 + (\psi_0/\psi_i)} \quad (2A)$$

In electron rich operation, the particle balance equation for electrons is

$$\frac{1}{4} n_e(0) \bar{v}_e = J_e(T_s) \exp \left[-|q \phi_p| / kT_s \right], \quad (\phi_p < 0) \quad (3A)$$

where $n_e(0) = n_i(0) = n_1$ is the density near the hot plate surface, \bar{v}_e is the electron thermal velocity, q is the electron charge (magnitude), ϕ_p is the plasma potential relative to the hot plate potential and J_e is the Richardson electron emission flux

$$J_e = C T_s^2 \exp(-q \phi_{we} / kT_s) \quad (4A)$$

where the constant $C \approx 3.8 \times 10^{20} \text{ cm}^{-2} \text{ sec}^{-1} \cdot \text{K}^{-2}$. Eq. 3A can be solved for the plasma potential (equal to the sheath potential difference at the hot plate):

$$\phi_p = \frac{kT_s}{q} \ln\left(\frac{n_1}{n_0}\right) \quad (5A)$$

where $n_0(T_s) = 4J_e(T_s)/\bar{v}_e$.

In electron rich operation, the hot plate sheath represents a potential barrier for ions returning from the plasma. Depending on the ion temperature T , a certain fraction of ions given by the factor $\exp[-|q\phi_p|/kT]$ can penetrate the barrier, of which a fraction $(1-P)$ recombine at the hot plate surface. The net flux F_{rec} of ions lost to the hot plate by surface recombination in electron rich operation is given by

$$F_{\text{rec}} = \frac{1}{4} n_1 \bar{v}_i e^{-\frac{q\phi_p}{kT}} (1-P), \quad (\phi_p < 0) \quad (6A)$$

The typical hot plate temperature in the multiple mirror experiment was $T_s = 2700^\circ \text{ K}$, for which $n_0 \approx 10^{12} \text{ cm}^{-3}$. With the typical density used in the confinement experiments, $n_1 \approx 10^{10} \text{ cm}^{-3}$, Eq. 5A gives $\phi_p \approx -4.6 kT_s/q \approx -1 \text{ volt}$. An ion temperature $kT \approx 2 kT_s \approx .4 \text{ eV}$ is calculated in Appendix B, giving a sheath attenuation factor

$\exp(-|q\phi_p|/kT) \approx .09$. For lithium at $T_s = 2700^\circ \text{ K}$, $1 - P \approx .9$, and Eq. 6A gives $F_{\text{rec}} \approx (.08)(\frac{1}{4} n_1 \bar{v}_i)$. With K multiple mirror cells, the loss flux to the collector is approximately $(\frac{1}{4} n_1 \bar{v}_i)/K$. With lithium and $K = 5$ cells, F_{rec} is approximately 30% of the collector flux. With potassium, and $K = 5$, $1 - P \approx .3$, and F_{rec} is approximately 10% of the collector flux which can be neglected.

APPENDIX B. Ion Temperature and Mean Free Path

To estimate the ion temperature T relative to the hot plate temperature T_s , in the presence of a sheath in electron rich operation, one uses the particle and energy balance equations for the ion species, of the form

$$\left[\left(F_o + \frac{1}{4} n \bar{v} - \frac{|q\phi_p|}{kT} \right) P \right] - \frac{1}{4} n \bar{v} - \frac{|q\phi_p|}{kT} = MF \quad (1B)$$

$$\left[\left(F_o + \frac{1}{4} n \bar{v} - \frac{|q\phi_p|}{kT} \right) P \right] (2kT_s + |q\phi_p|) - \frac{1}{4} n \bar{v} - \frac{|q\phi_p|}{kT} (2kT + |q\phi_p|) = MQ. \quad (2B)$$

Here F_o is the neutral flux bombarding the hot plate from the oven, n , \bar{v} and T are the ion density, thermal velocity and temperature near the hot plate, and ϕ_p is the plasma potential given by Eq. 6A. Eq. 1B, applied at the hot plate side of the sheath, and Eq. 2B, applied at the plasma side of the sheath, are statements that the difference in total particle and energy fluxes at the hot plate are equal to the net particle flux MF and net energy flux MQ , respectively. The mirror ratio M is inserted because the source is in the mirror throat and we wish to reference F and Q to the midplane. These net fluxes are associated with radial loss and losses to the collector. Eliminating the quantity in square brackets between Eq. 1B and Eq. 2B results in

$$\frac{1 + \left[\frac{MF}{\frac{1}{4} n \bar{v}} \right] \left[e^{+\frac{|q\phi_p|}{kT}} \right] \left(1 + \frac{|q\phi_p|}{2kT_s} \right)}{1 + \left[\frac{MQ}{2kT \left(\frac{1}{4} n \bar{v} \right)} \right] \left[e^{+\frac{|q\phi_p|}{kT}} \right]} (\phi_p < 0) \quad (3B)$$

F can be evaluated in terms of $\tau_{mm}(\text{max})$ and F_{min} of Ref. 1 according to

$$F = \frac{\tau_{mm}(\text{max})}{\tau_t} F_{\text{min}} \quad (4B)$$

where τ_{tot} , measured experimentally, is less than $\tau_{mm}(\text{max})$ due to radial loss, ambipolar effects, MHD effects, and incomplete scattering in each cell. Q is given in terms of KTF in Fig. 2 of Ref. 1. Defining the ratio

$$\mu \equiv Q/kTF \quad (5B)$$

we find $2 < \mu < 4$ depending on the mfp regime. Substituting Eq. 4B with (with $MF_{\text{min}} = \frac{1}{4} n\bar{v}/K$), and Eq. 5B into Eq. 3b, we obtain

$$\frac{T}{T_s} = \frac{1 + K_{\text{eff}}^{-1} e^{\frac{|q\phi_p|}{kT}} + \frac{|q\phi_p|}{kT} \left(1 + \frac{|q\phi_p|}{2kT_s}\right)}{1 + \mu K_{\text{eff}}^{-1} e^{\frac{|q\phi_p|}{kT}} + \frac{|q\phi_p|}{kT}}, \quad (\phi_p < 0) \quad (6B)$$

where

$$K_{\text{eff}} \equiv \left[\frac{\tau}{\tau_{mm}(\text{max})} \right] K \quad (7B)$$

Taking $\mu = 3$, which is the approximate experimental condition, Eq. (6B) can be evaluated graphically for the ratio T/T_s as a function of ϕ_p for various \bar{K}_{eff} . Using Eq. 6A for ϕ_p , the results for T/T_s are plotted in Fig. B1 as a function of n_1/n_0 for $K_{\text{eff}} = 1, 5, 10, 100$ and ∞ . For $K_{\text{eff}} < 5$, the values of T/T_s are fortunately insensitive to K_{eff} ,

and for 10% accuracy, Eq. 4B for F need not be evaluated. Note that for n_1/n_0 near 1, and small K , $T < T_s$, a result of the preferential and loss of fast ions cooling the plasma. At $n_1/n_0 \approx 10^{-2}$, the typical experimental operating point, however, Fig. B1 predicts $T \approx 2 T_s$, a result of the thermalization of the energy imparted to the ions by the hot plate sheath. The ion-ion mfp λ for scattering into a root mean square angle of one radian is plotted in Fig. B2 as a function of density n_1 at the source for various hot plate temperatures T_s , using Eq. 6A and Fig. 1B for T/T_s . For λ at $z \neq 0$ where $n(z) < n_1$, the values of λ in Fig. B2 can be multiplied by $n_1/n(z)$.

Appendix C Correction Factors for Effects of Radial Loss on τ_z

Consider a symmetric multiple-mirror system of half length $L/2$ containing K mirror cells numbered $j = 1, 2 \dots K$ starting from the center cell, into which $2S$ particles are injected. We assume a constant rate of radial loss proportioned to density n_j in each cell:

$$\frac{dn_j}{dt} \text{ radial} = - \epsilon n_j \quad (1C)$$

where $\epsilon \equiv \tau_{\text{rad}}^{-1}$. For particle balance in cell j , with M , A and \bar{v} constant,

$$\frac{1}{4}n_{j-1}\bar{v} + \frac{1}{4}n_{j+1}\bar{v} = \frac{1}{2}n_j\bar{v} + M\ell_c n_j \epsilon \quad (2C)$$

Note that n_{j+1} should be taken 0 for $j = K$. For cell $j = 1$, Eq. 2C is given by

$$S + \frac{1}{4}n_2\bar{v} = \frac{1}{4}n_1\bar{v} + M\ell_c n_1 \epsilon \quad (3C)$$

The effects of surface recombination loss can be included by the use of an effective source strength S' given by

$$S' = S - F_{\text{rec}} \quad (4C)$$

For a given ϵ , Eqs. 2C and 3C give K equations for K unknown densities. The solutions for a 10 cell system and for $\epsilon = 0$, $\epsilon = \tau_{\text{mm}}^{-1}(\text{max})$ and $\epsilon = 2\tau_{\text{mm}}^{-1}(\text{max})$ are given in Fig. 1C. The densities are in units of $(4S'/\bar{v})$. Assuming the collector signals $I_c(L')$ are proportional to n_{10} in the last cell in each case, τ_z is proportional to $\sum_{j=1}^{10} n_j/n_{10}$.

Since all n_j are proportional to S' , τ_z is independent of S' . Fig. C1 shows radial loss reduces n_{10} by a larger factor than $\sum_{j=1}^{10} n_j$ is reduced. Thus τ_z for $\epsilon \neq 0$ is greater than $\tau_{mm}(\text{max})$ for $\epsilon = 0$. Assuming surface recombination loss is negligible compared to radial loss, or that a certain portion of the collector current drop due only to radial loss $I_c(0)/I_c(L)$ (radial) is distinguishable, for each curve in Fig. C1 with a given ϵ there is a corresponding value of

$$\frac{I_c(0)}{I_c(L')} = \frac{n_K(\epsilon=0)}{n_K(\epsilon)} \quad (5C)$$

The ratio of τ_z to $\tau_{mm}(\text{max})$ defined by

$$\zeta \equiv \frac{\tau_z}{\tau_{mm}(\text{max})} = \frac{\sum_{j=1}^{10} (n_j/n_K)(\epsilon)}{\sum_{j=1}^{10} (n_j/n_K)(\epsilon=0)} \quad (6C)$$

is plotted as a function of $I_c(0)/I_c(L')$ in Fig. C2 for a 10 cell and a 5 cell system. Assuming both τ_z and τ_{mm} for a non optimum mfp experiment are less than for the ideal short mfp system by the same amount, the calculated ratios ζ given in Fig. C2 will also apply to the experiment. That is, an experimental value of $\tau_{mm}(\text{exp})$ is obtained from measured values of $\tau_z(\text{exp})$ by

$$\tau_{mm}(\text{exp}) = \zeta \tau_z(\text{exp}) \quad (7C)$$

$\tau_{mm}(\text{exp})$ is the appropriate experimental quantity to compare with $\tau_{mm}(\text{max})$.

To treat the limiting case of many cells, the one dimensional diffusion equation (constant D)

$$D \frac{d^2 n}{dz^2} - \epsilon n = 0 \quad (8C)$$

can be solved to obtain a correction factor

$$\zeta \equiv \frac{\tau_z}{\tau_{mm}} = \frac{\int_0^L n(z) dz}{\left(-D \frac{dn}{dz} \Big|_{z=L'} \right) (L^2/2D)} \quad (9C)$$

with the boundary conditions $n(L') = 0$ (absorbing boundary at $z = L'$) and $-D \frac{dn}{dz} \Big|_{z=0} = S'$. The result is given as the diffusion theory line in Fig. 2C. Diffusion theory represents the limiting values of ζ for many cells in which the density profiles and radial loss are continuous. The values of ζ increase with fewer finite number of cells, due to an increasing effect of the assumed discrete distribution of radial loss for those cases.

REFERENCES

1. A. Makhijani, A. J. Lichtenberg, M. A. Lieberman, and B. G. Logan, Phys. Fluids, this issue.
2. B. Grant Logan, I. G. Brown, M. A. Lieberman and A. J. Lichtenberg, Phys. Rev. Lett. 29 1435 (1972).
3. B. Grant Logan, A. J. Lichtenberg, M. A. Lieberman and A. Makhijani, Phys. Rev. Lett. 28 144 (1972).
4. B. Grant Logan, "Extrapolated Parameters for a Pulsed, Cusp Ended Thermonuclear Reactor," Masters Thesis in Nuclear Engineering, University of California, Berkeley (1969).
5. D. J. Rose, Oak Ridge National Laboratory Report TM-2204 (1968).
6. D. J. Rose and M. Clark, "Plasmas and Controlled Fusion", M.I.T. Press (1961).
7. A. J. Lichtenberg and B. Myers, Bul. Am. Phys. Soc., 17, 1058 (1972).
8. J. M. Dawson, H. P. Furth, and F. H. Tenney, Phys. Rev. Lett. 26 1156 (1971).
9. A. J. Lichtenberg, "Phase Space Dynamics of Particles", J. Wiley (1969), Sec. 5.5.

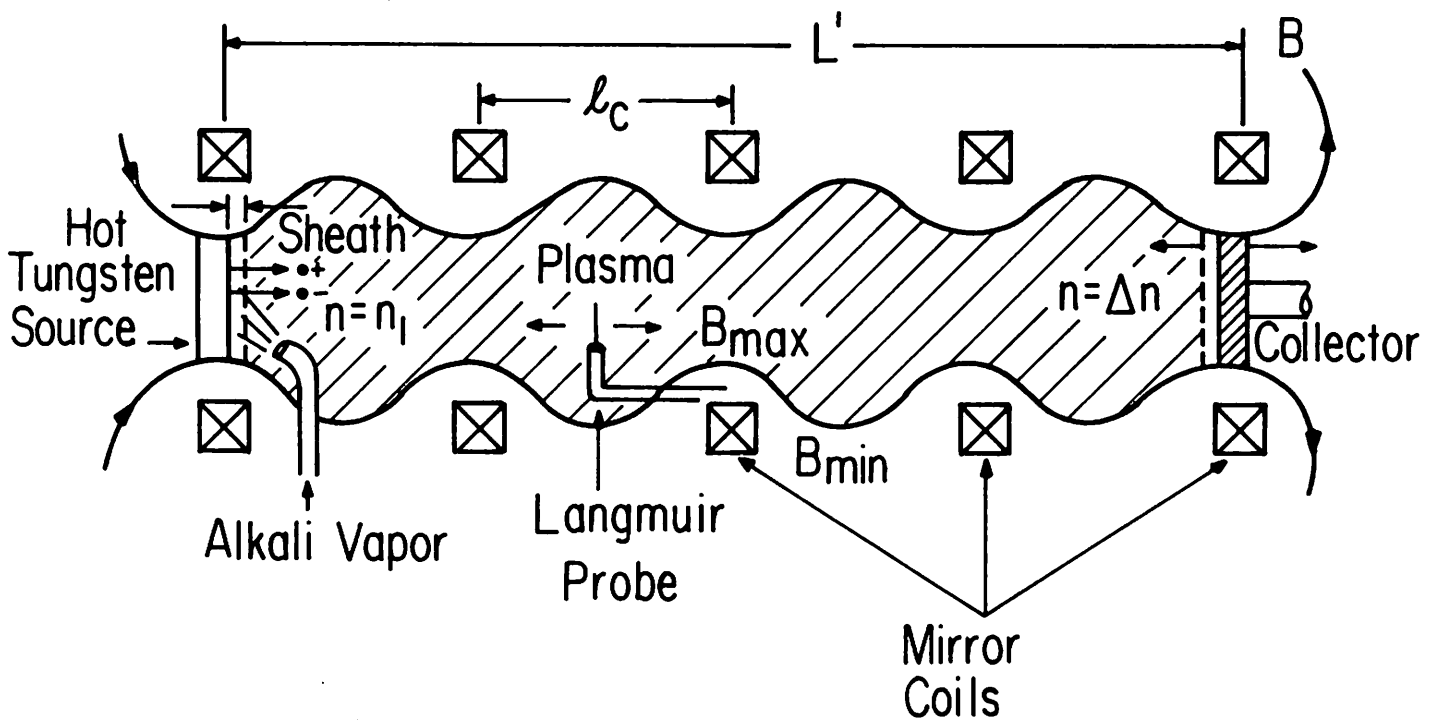


Fig. 1 The Multiple-Mirror Experiment

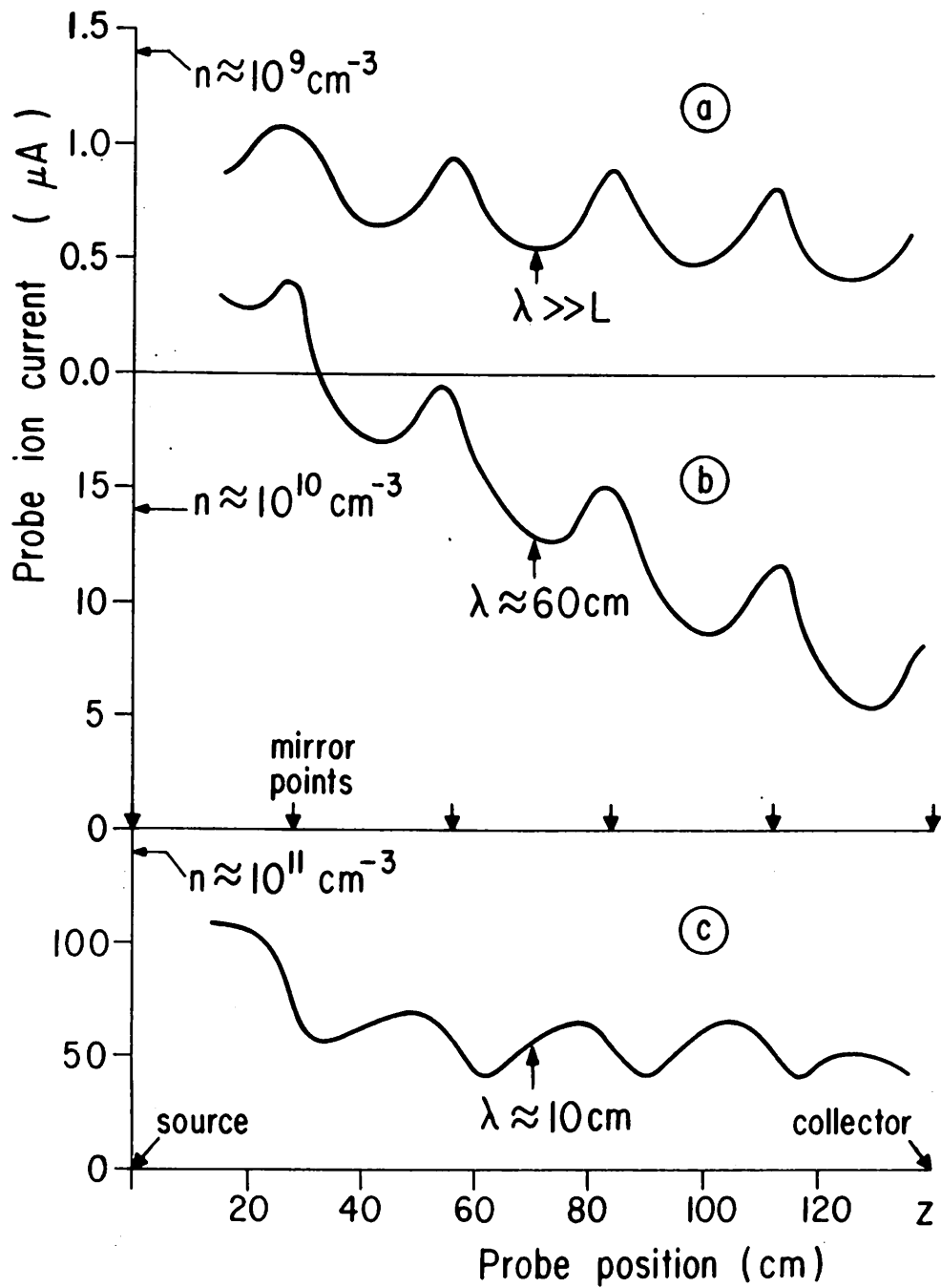


Fig. 2 Langmuir probe ion saturation current (density) as a function of axial position z , for (a) low, (b) intermediate, (c) high density regimes. Potassium, 5 cells.

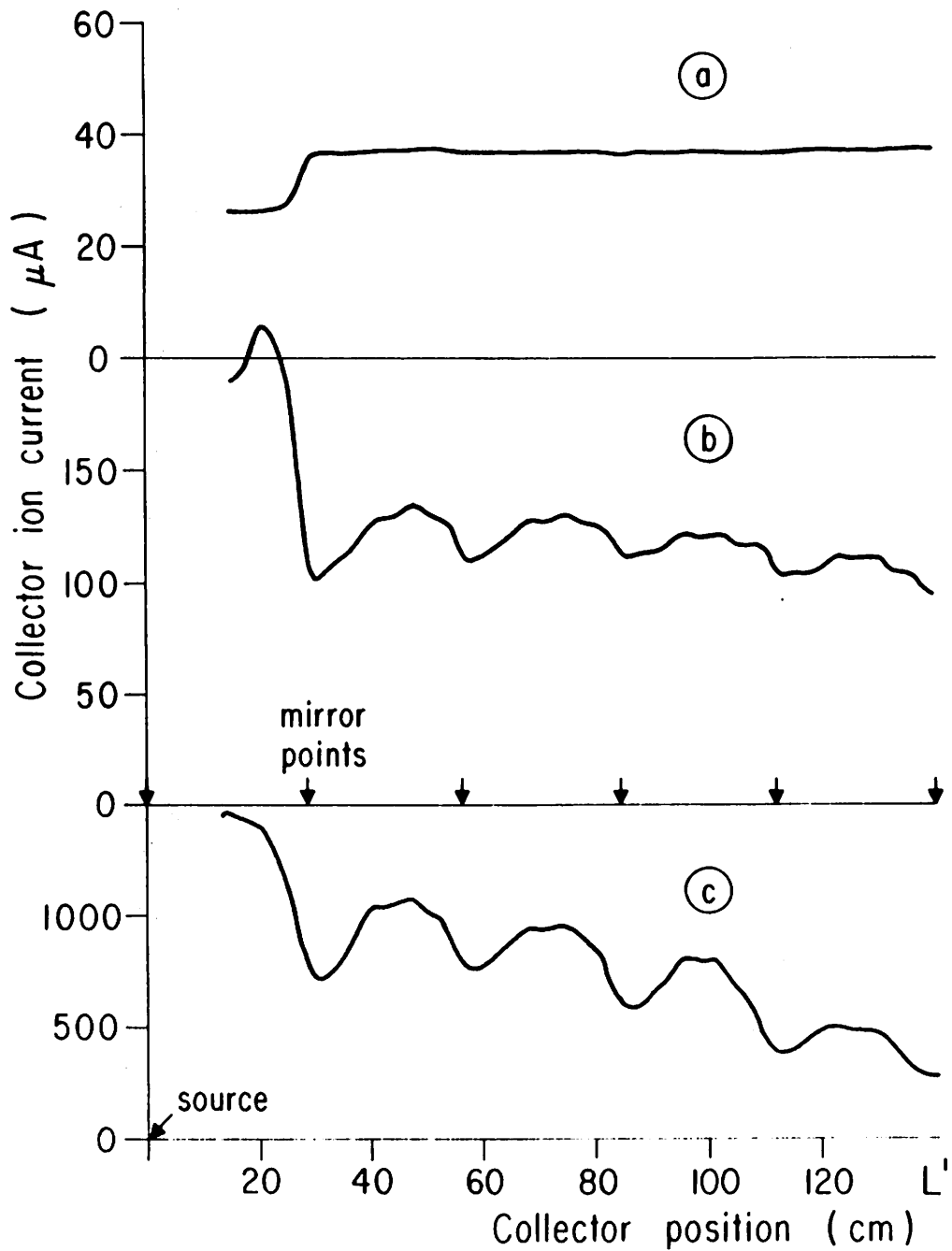


Fig. 3 Collector ion saturation current as a function of distance from the source for (a) low; (b) intermediate, (c) high density regimes. Potassium, 5 cells.

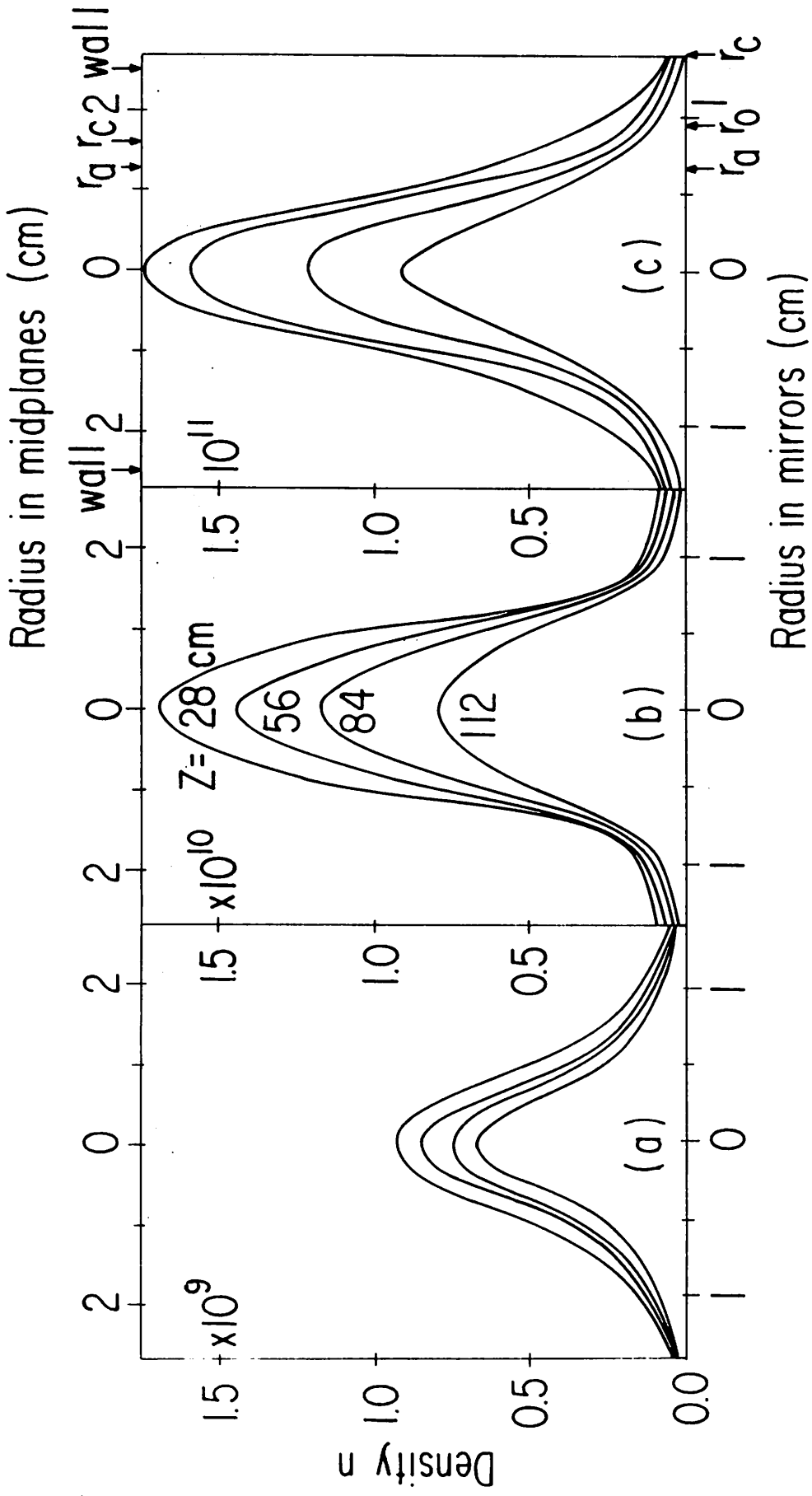


Fig. 4 Radial density profiles for (a) low density (b) intermediate density and (c) high density regimes

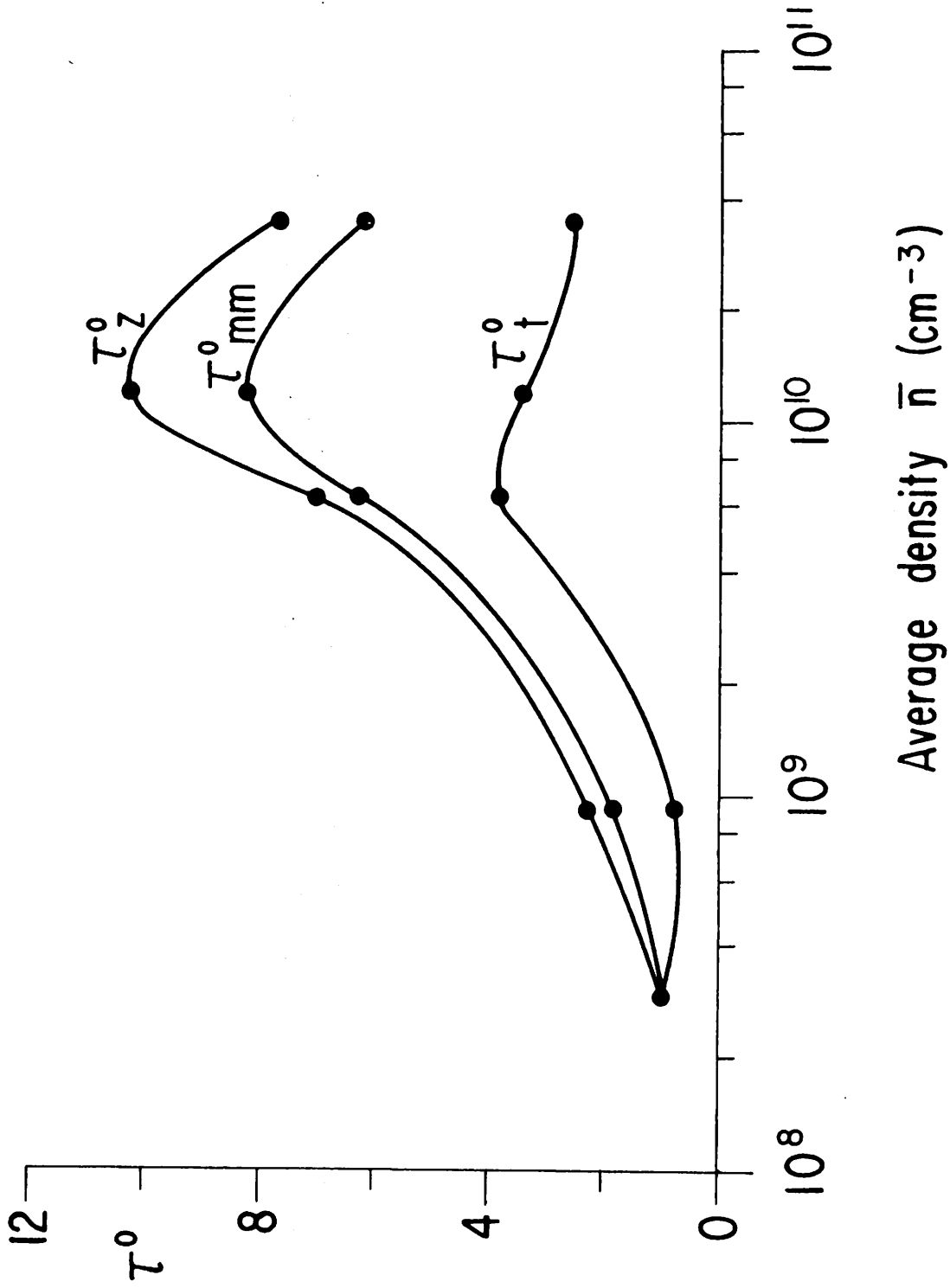


Fig. 5 Confinement times τ^0 , τ^0_{mm} , and τ^0_z (normalized to a transit time $L'/z\bar{v}$), as a function of average density \bar{n} for potassium, 5 cells, $M = 3.27$ (lower radial loss).

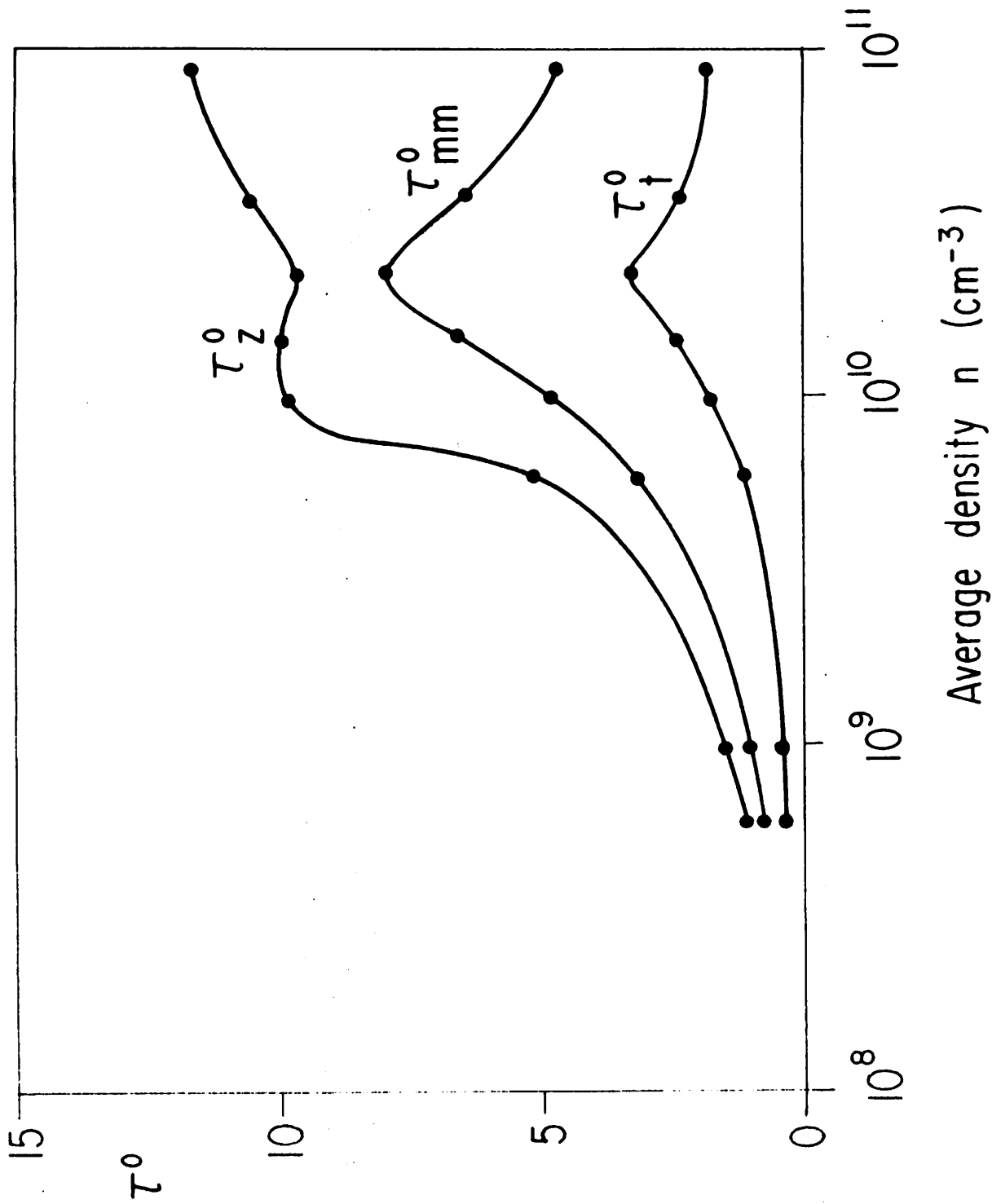


Fig. 6 Normalized confinement times τ_{tot}^0 , τ_z^0 , and τ_{mm}^0 as a function of average density \bar{n} . Potassium, 5 cells, $M = 3.7$ (higher radial loss)

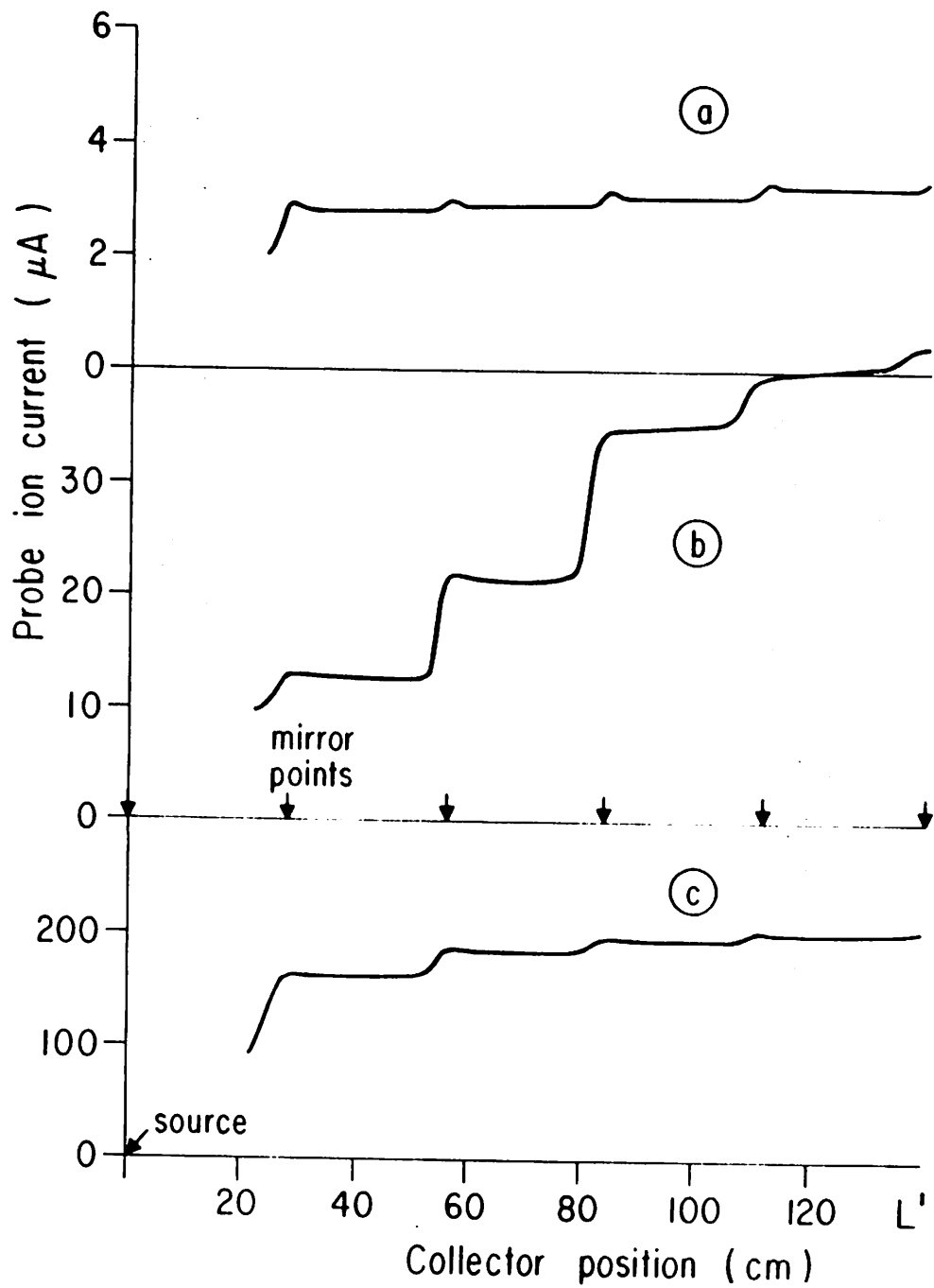


Fig. 7 Langmuir probe ion saturation current (density n_1) in the first cell as a function of collector position, in the (a) low density, (b) intermediate density, and (c) high density regimes. Potassium, 5 cells

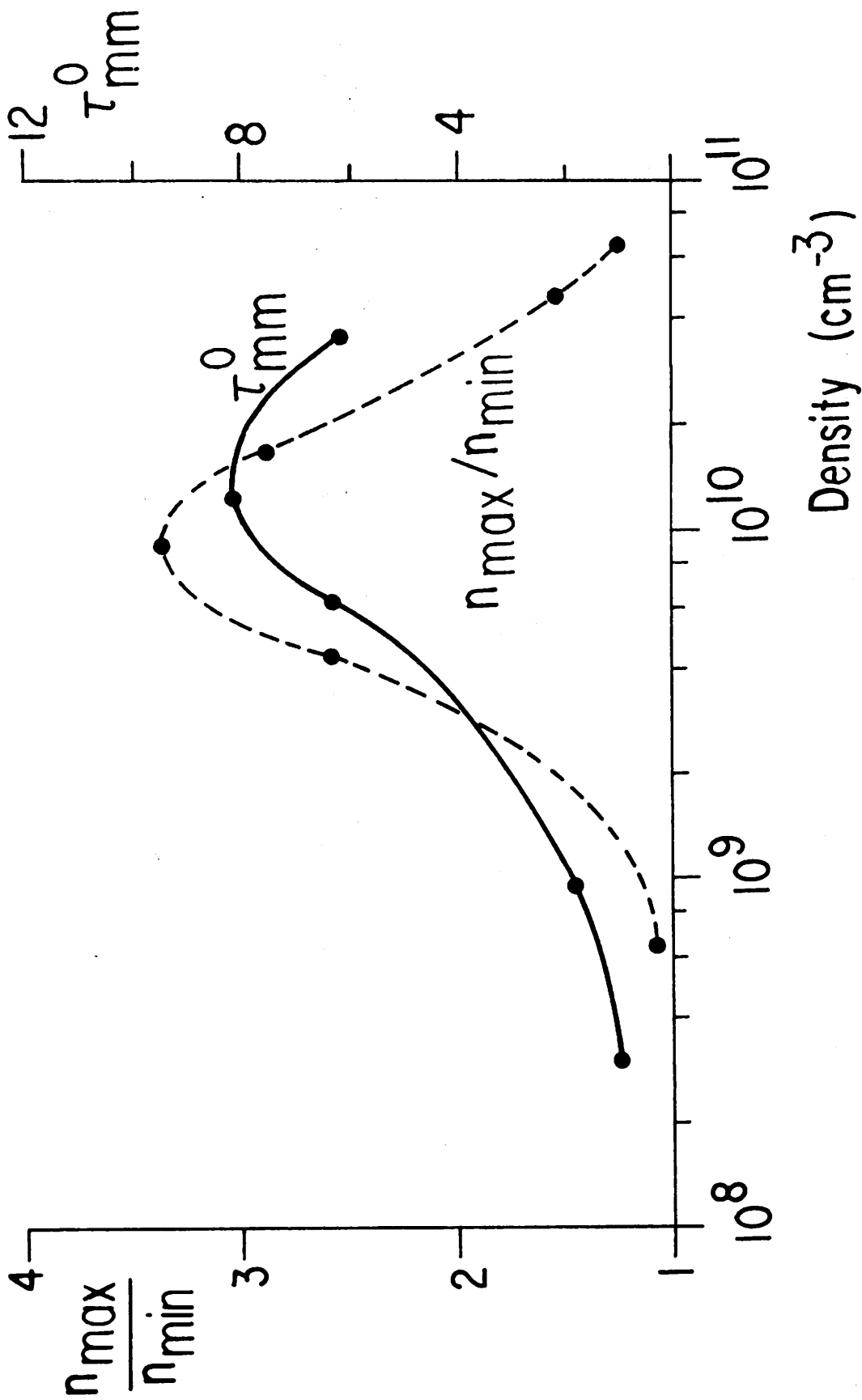


Fig. 8 First cell density ratio n_{\max}/n_{\min} (dashed line) as a function of $1/2 n_{\max}$ and τ_{mm}^0 (solid line as a function of average density \bar{n} . Potassium, 5 cells

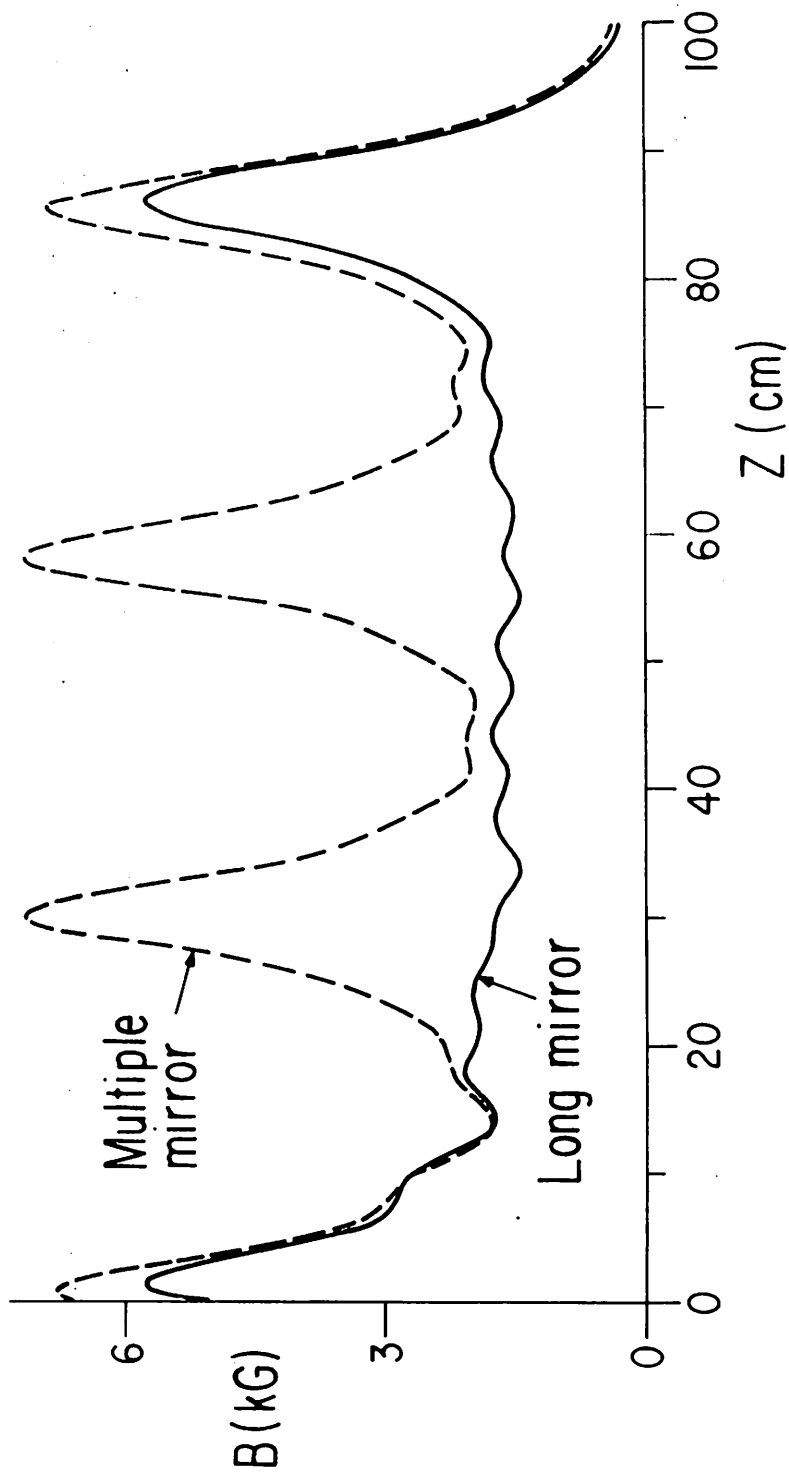


Fig. 9 Axial magnetic field profiles for the 3 cell multiple-mirror and for the long mirror.

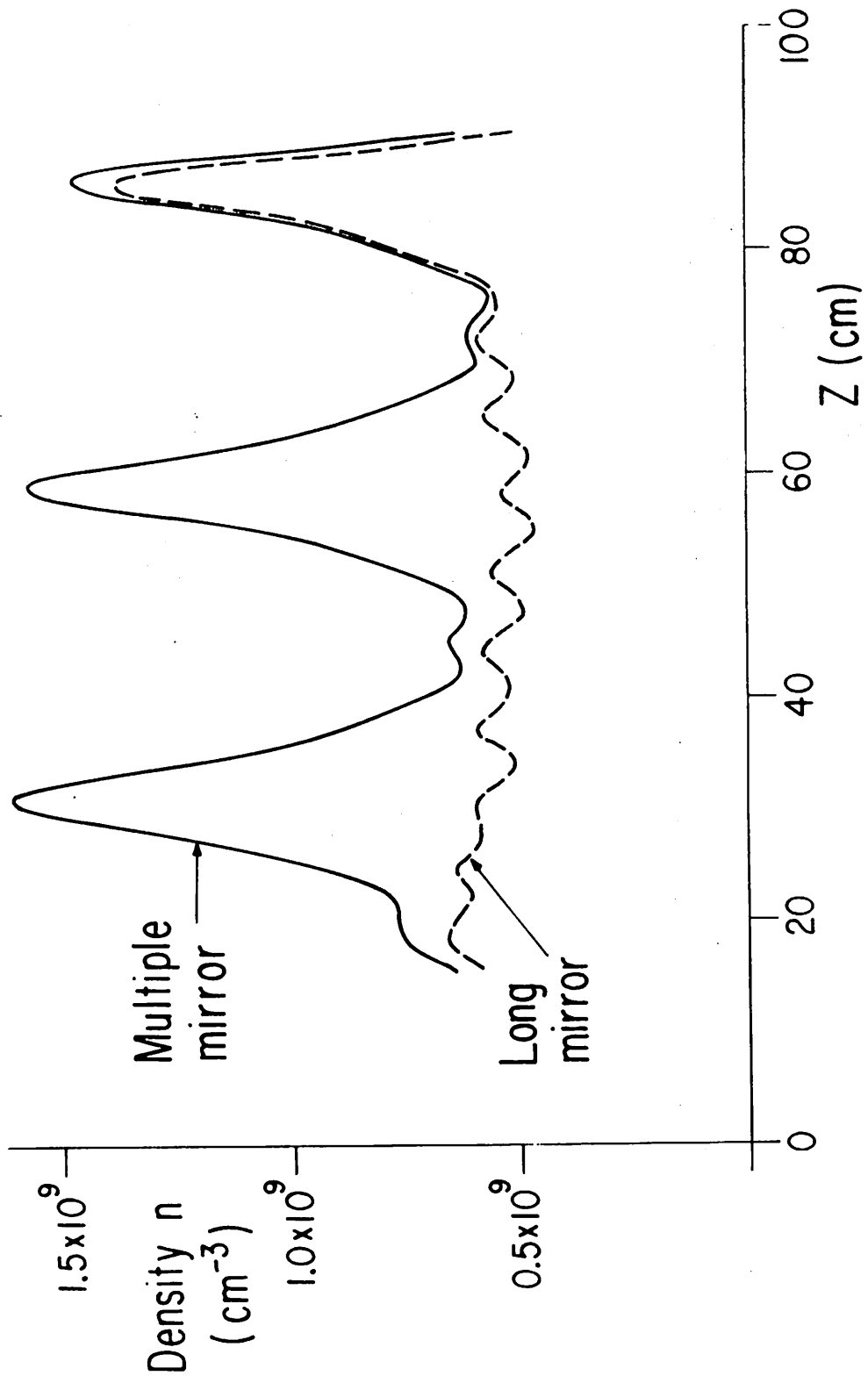


Fig. 10 3 cell (solid line) and long mirror (dashed line) density as a function of z for the low density regime. Potassium.

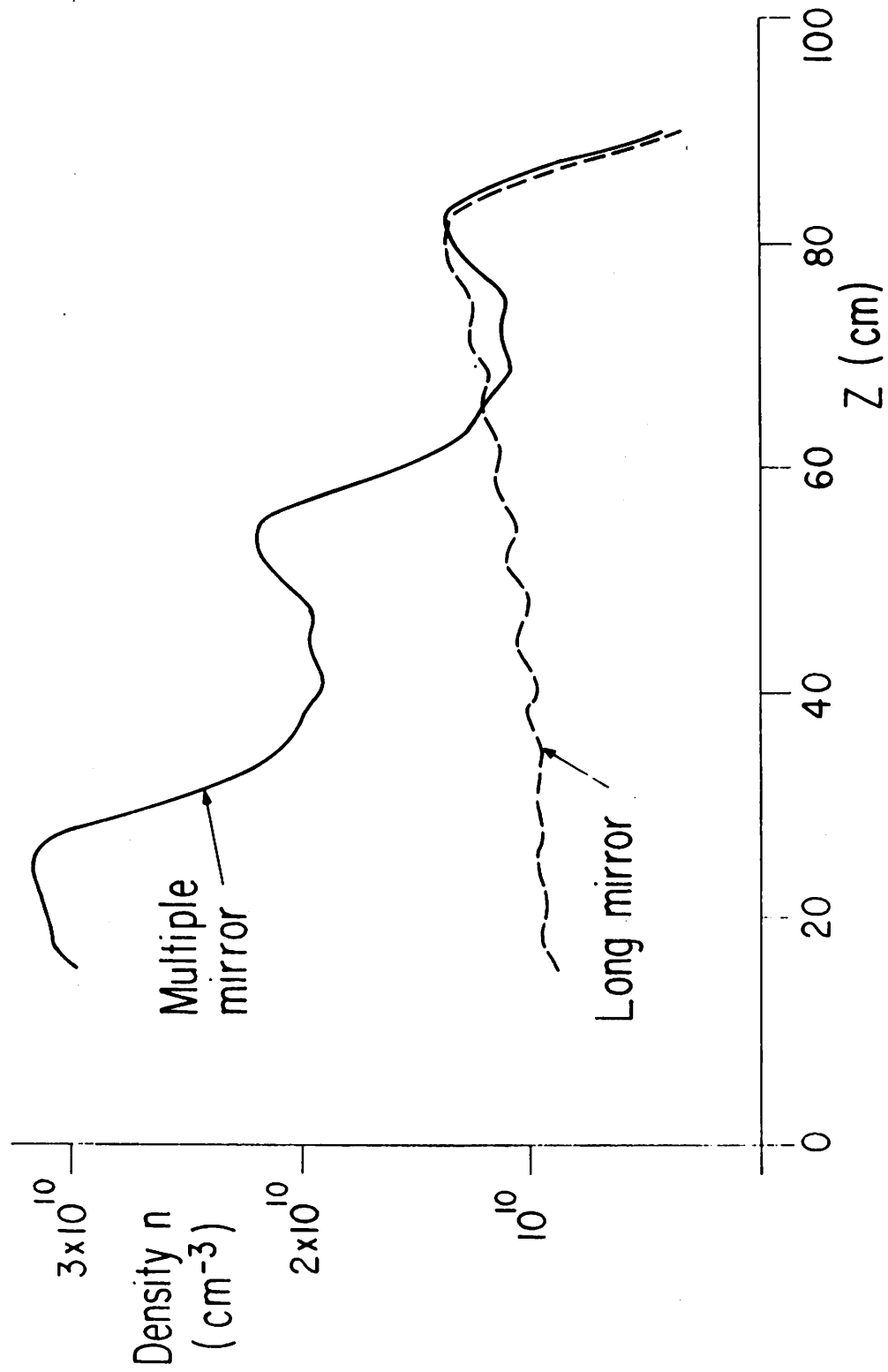


Fig. 11 3 cell (solid line) and long mirror (dashed line) density as a function of z for the intermediate density regime.

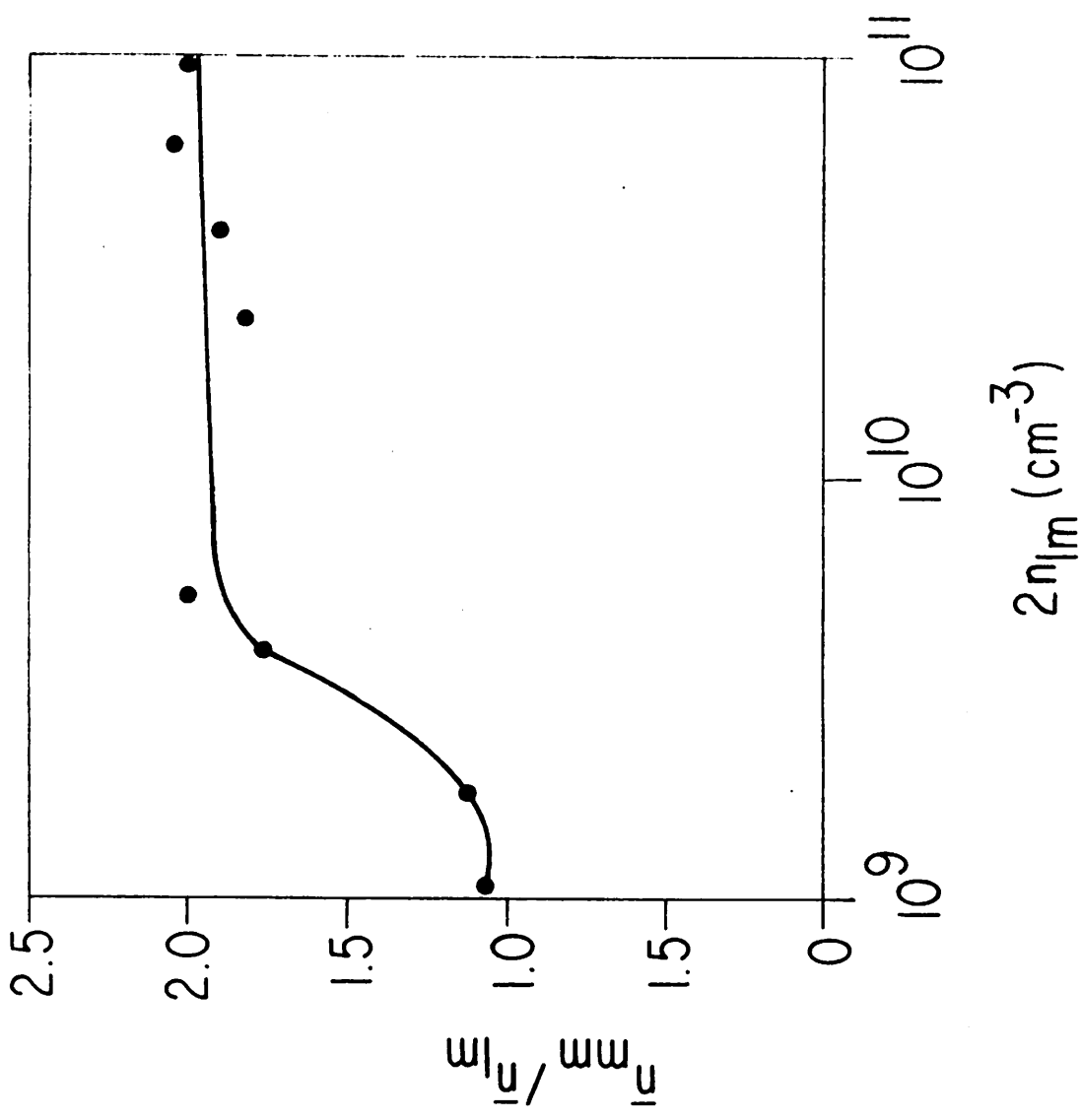


Fig. 12 Ratio of average multiple mirror midplane density \bar{n}_{mm} with 3 cells to the average long mirror midplane density $\bar{n}_{\rho m}$ as a function of twice the long mirror density $2 n_{\rho m}$. Potassium.

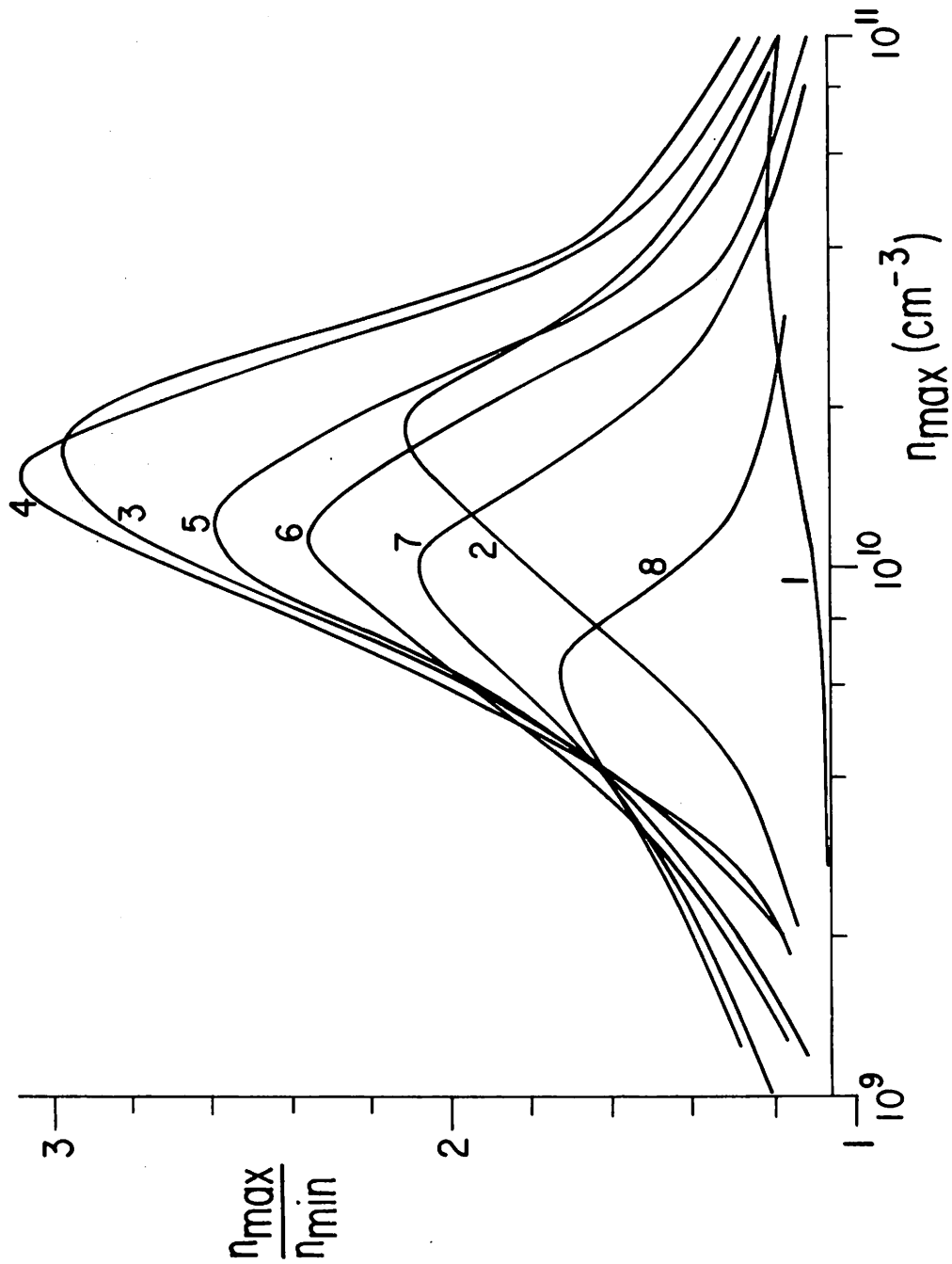


Fig. 13 First cell density ratio n_{\max}/n_{\min} as a function of n_{\max} for 8 different mirror ratios given in Table B. Potassium, 5 cells

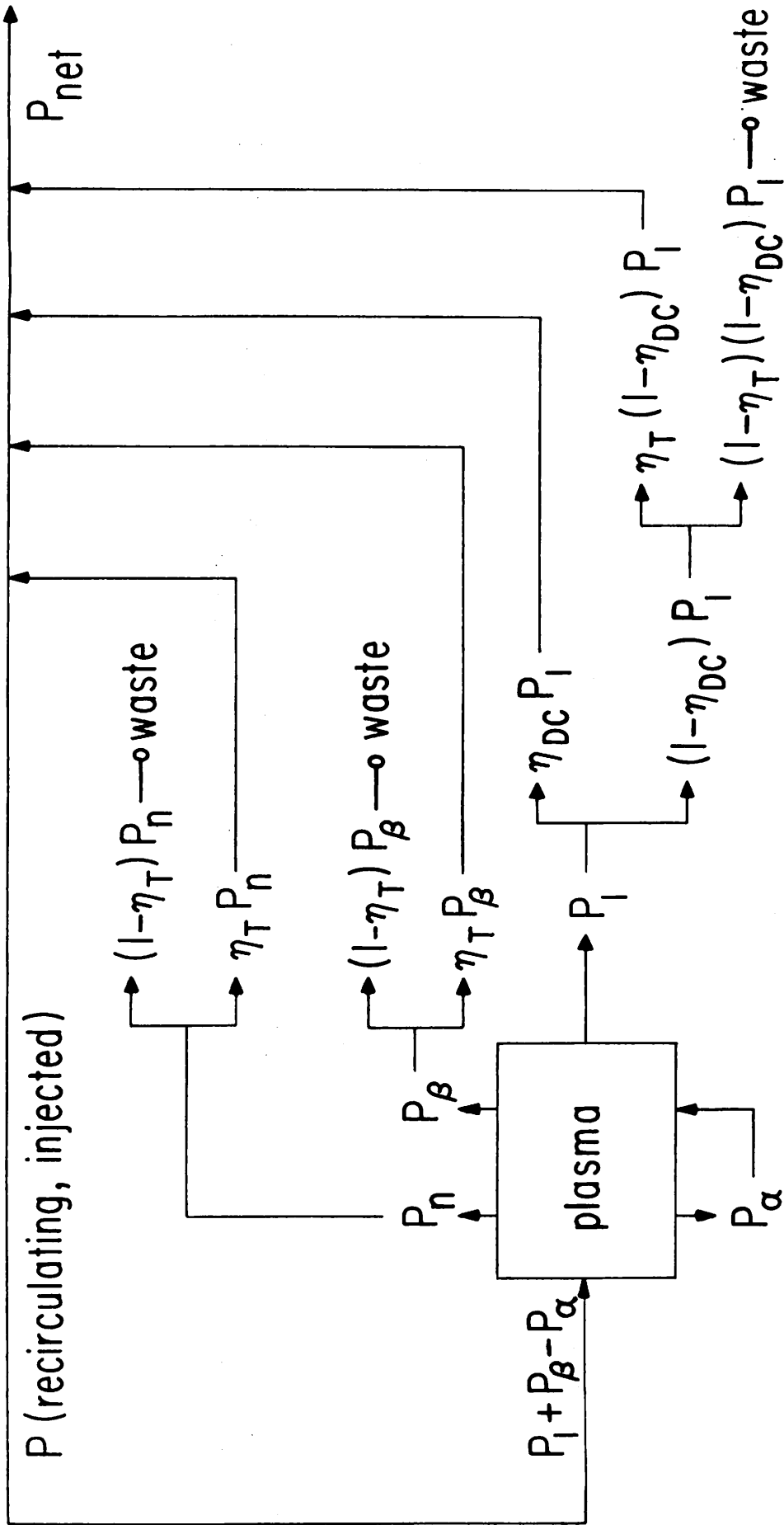


Fig. 14 Power Flow Diagram.

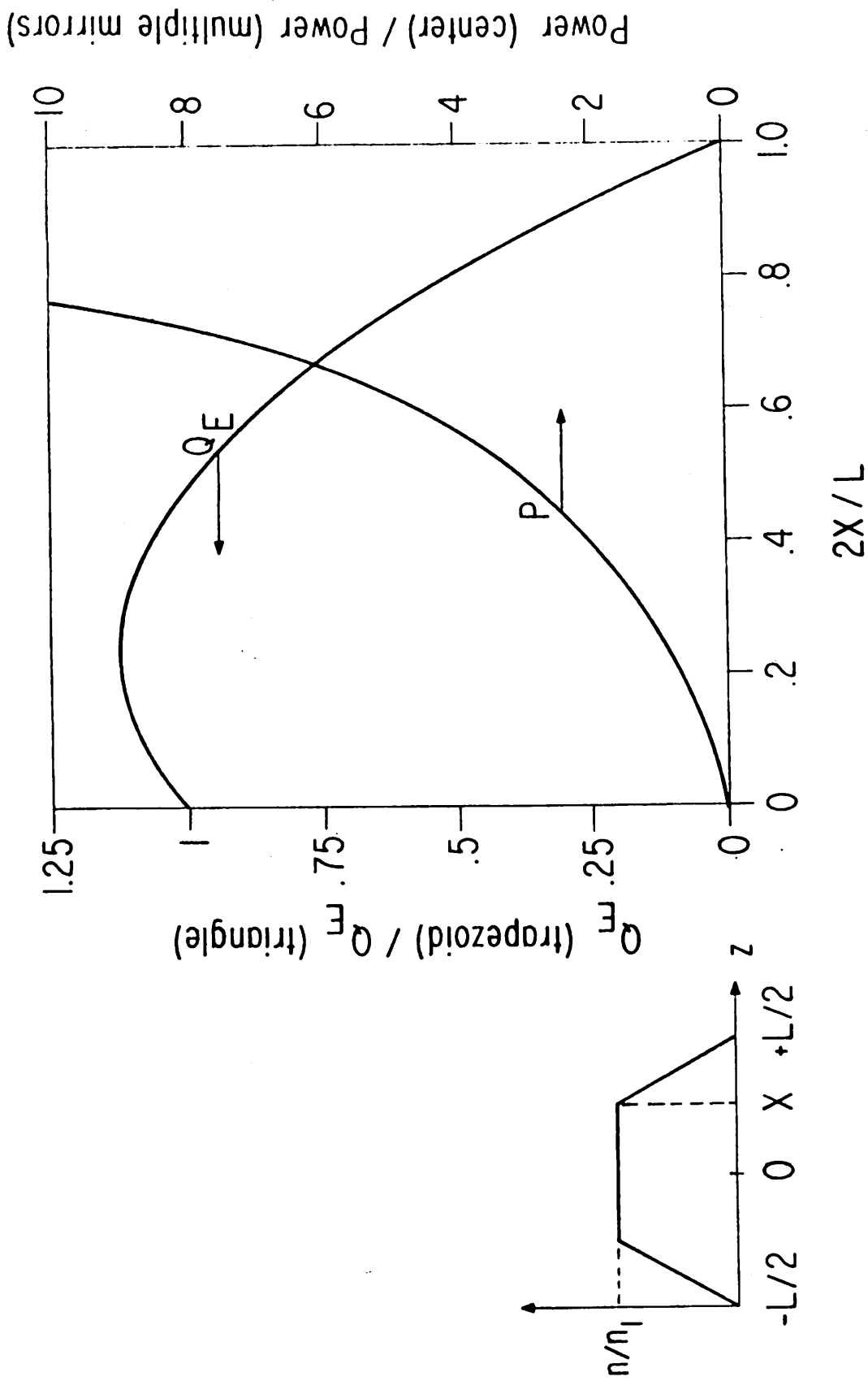


Fig. 15 Variation of Q_E and of ratio of power in center section to power in multiple mirror region for a trapezoidal density distribution with $L = \text{const.}$ and $n_1 = \text{const.}$ and varying ratio of length of constant density region to multiple mirror region.

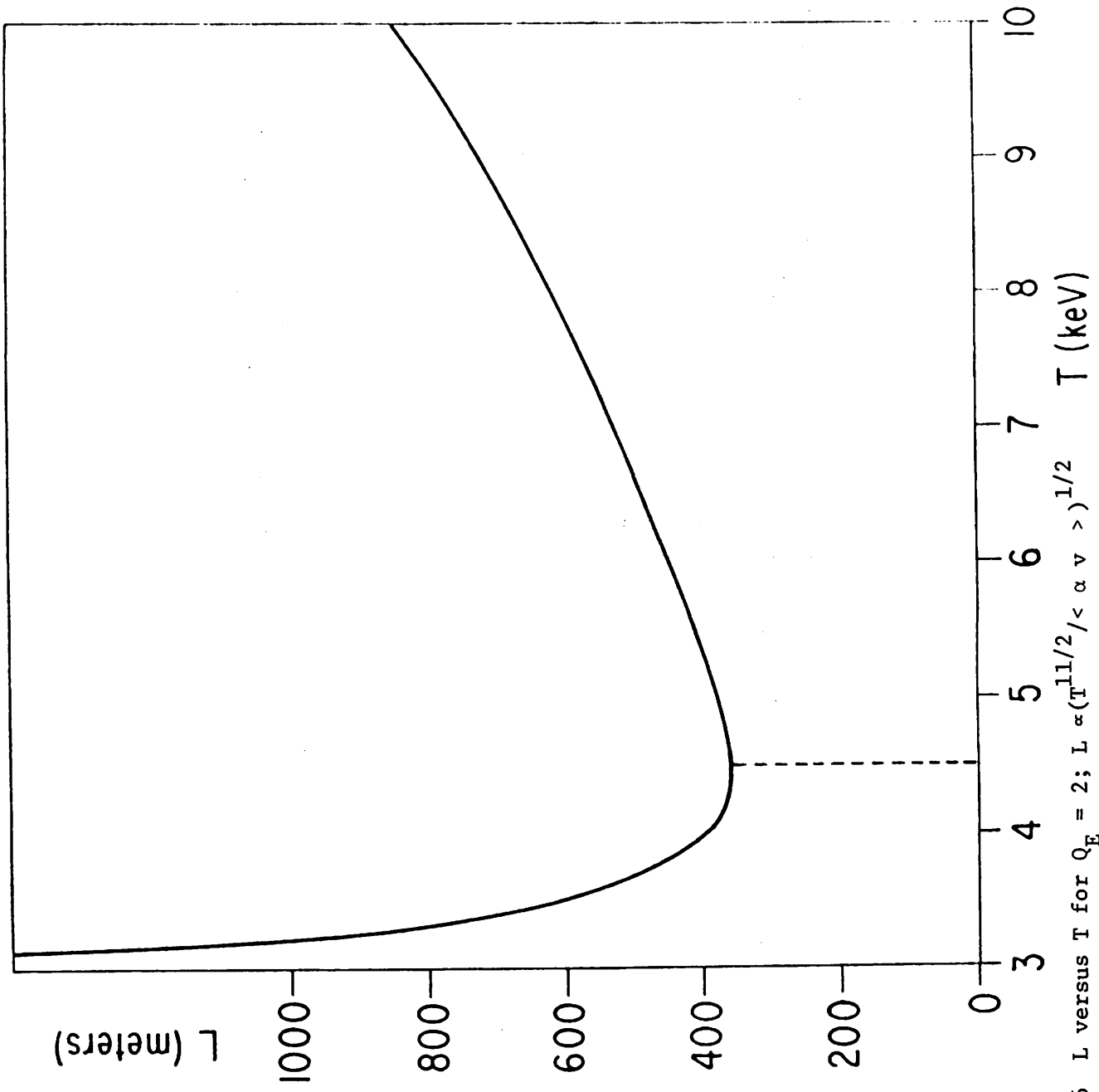


Fig. 16 L versus T for $Q_E = 2$; $L \propto (T^{11/2} / \langle \alpha v \rangle)^{1/2}$

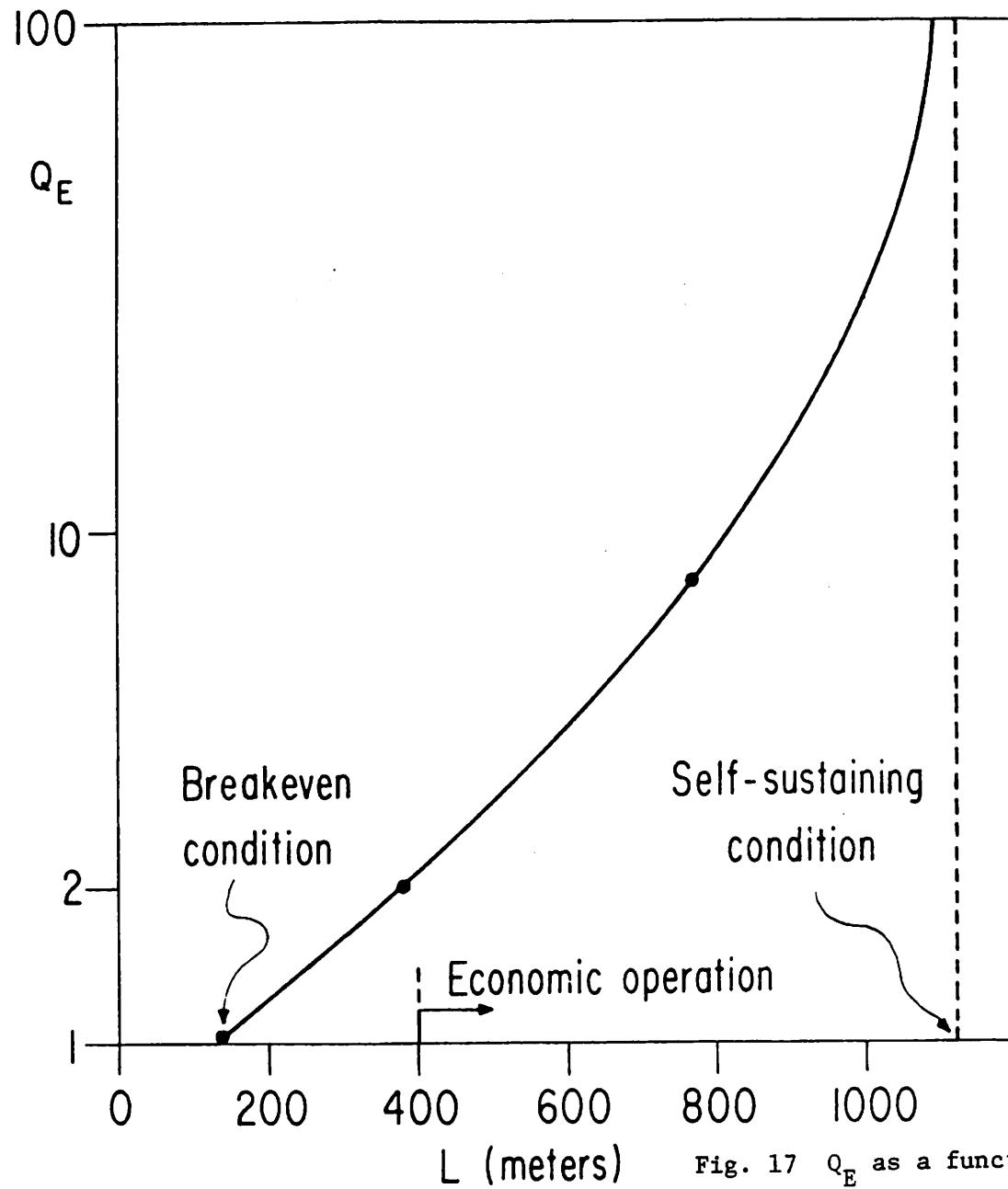


Fig. 17 Q_E as a function of total length L .

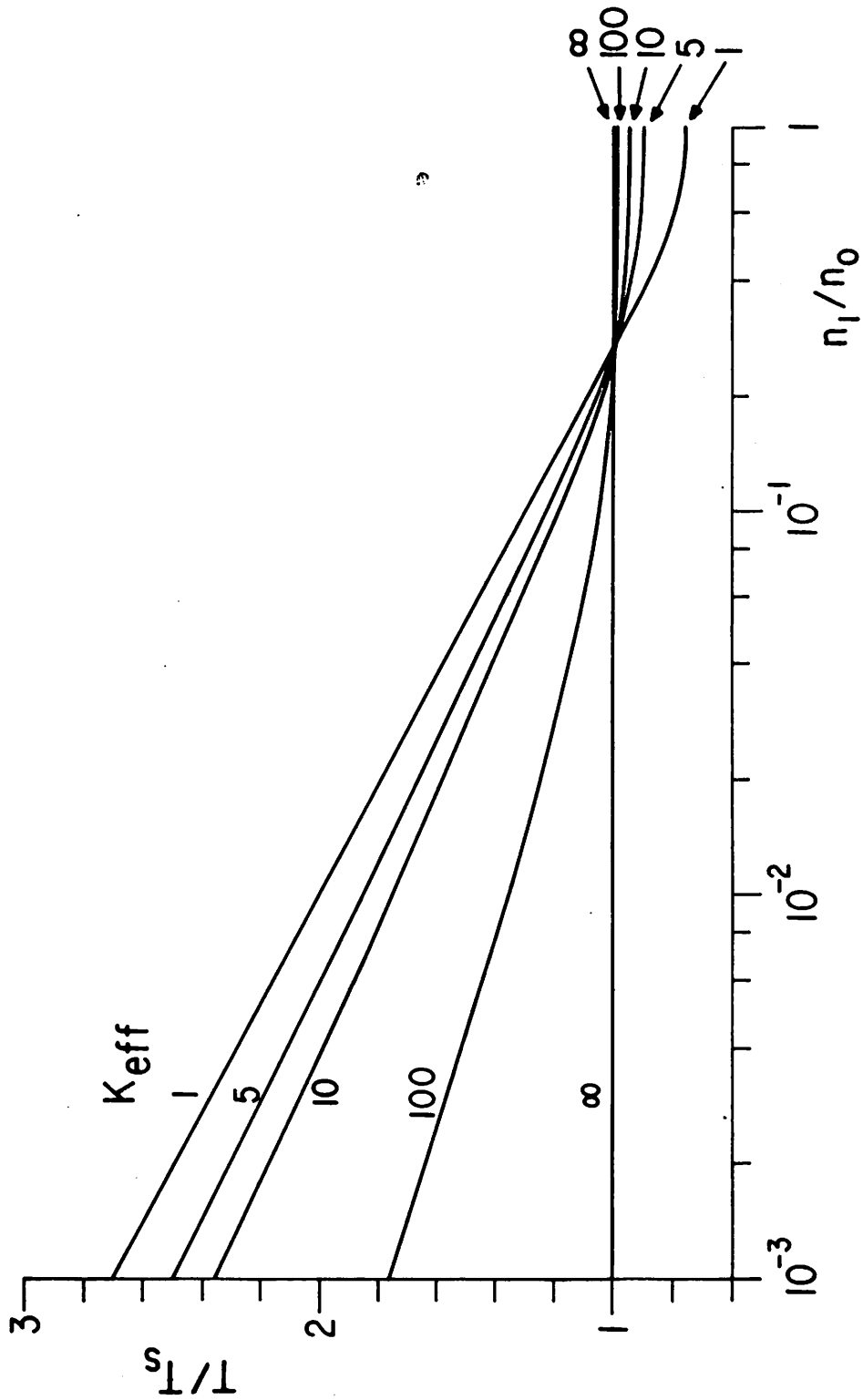


Fig. B1 (T/T_s) as a function of (n_1/n_0) for $\mu = 3$ ($Q = 3kTF$)

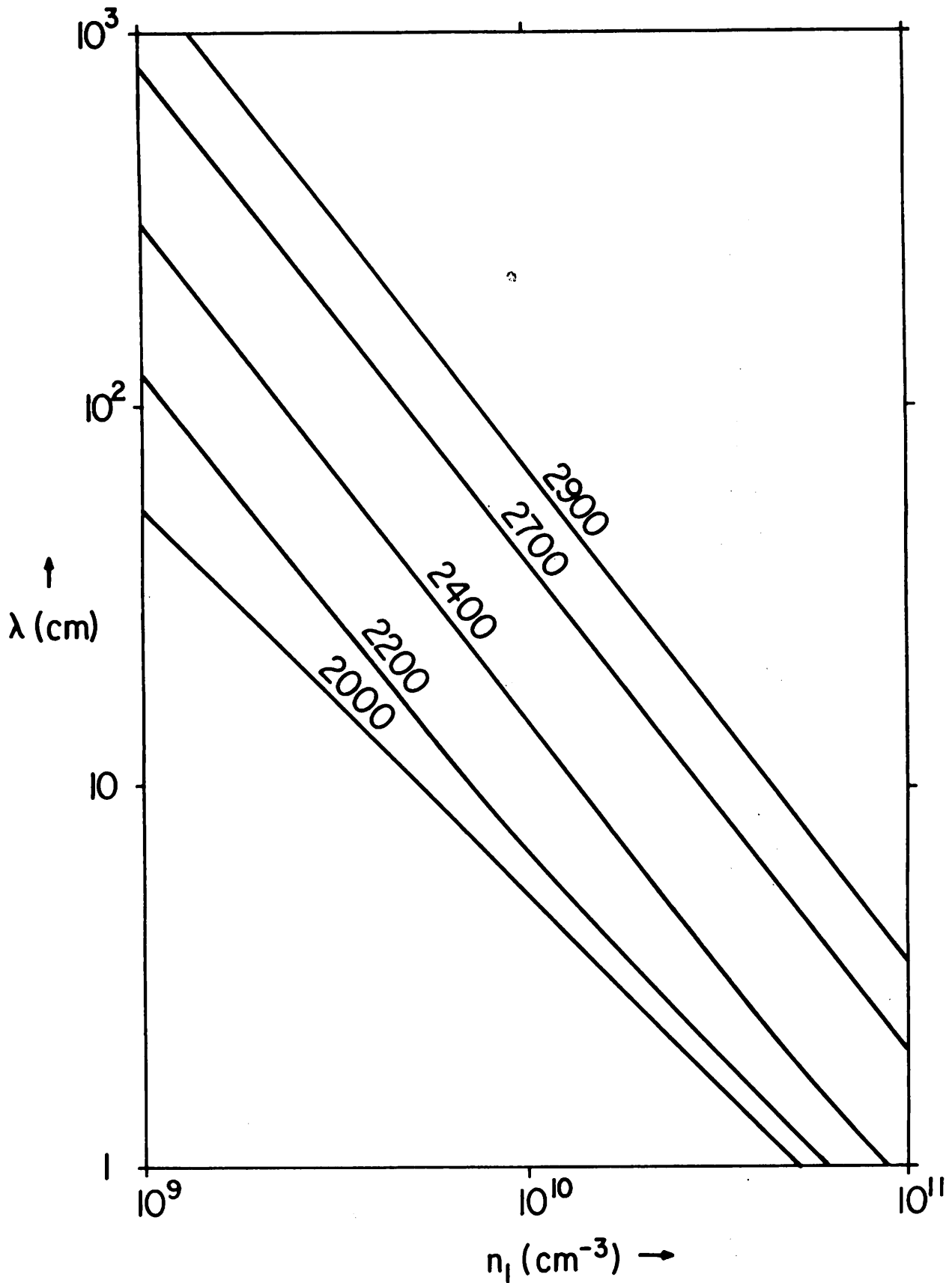


Fig. B2 Ion-ion mfp λ for thermal velocity ions as a function of density n_1 at the source ($z = 0$) for $\mu = 3$ ($Q = 3$ kTF), for $K_{\text{eff}} = 5$, and for hot plate temperatures T_s 2900, 2700, 2400, 2200 and 2000 $^{\circ}\text{K}$.

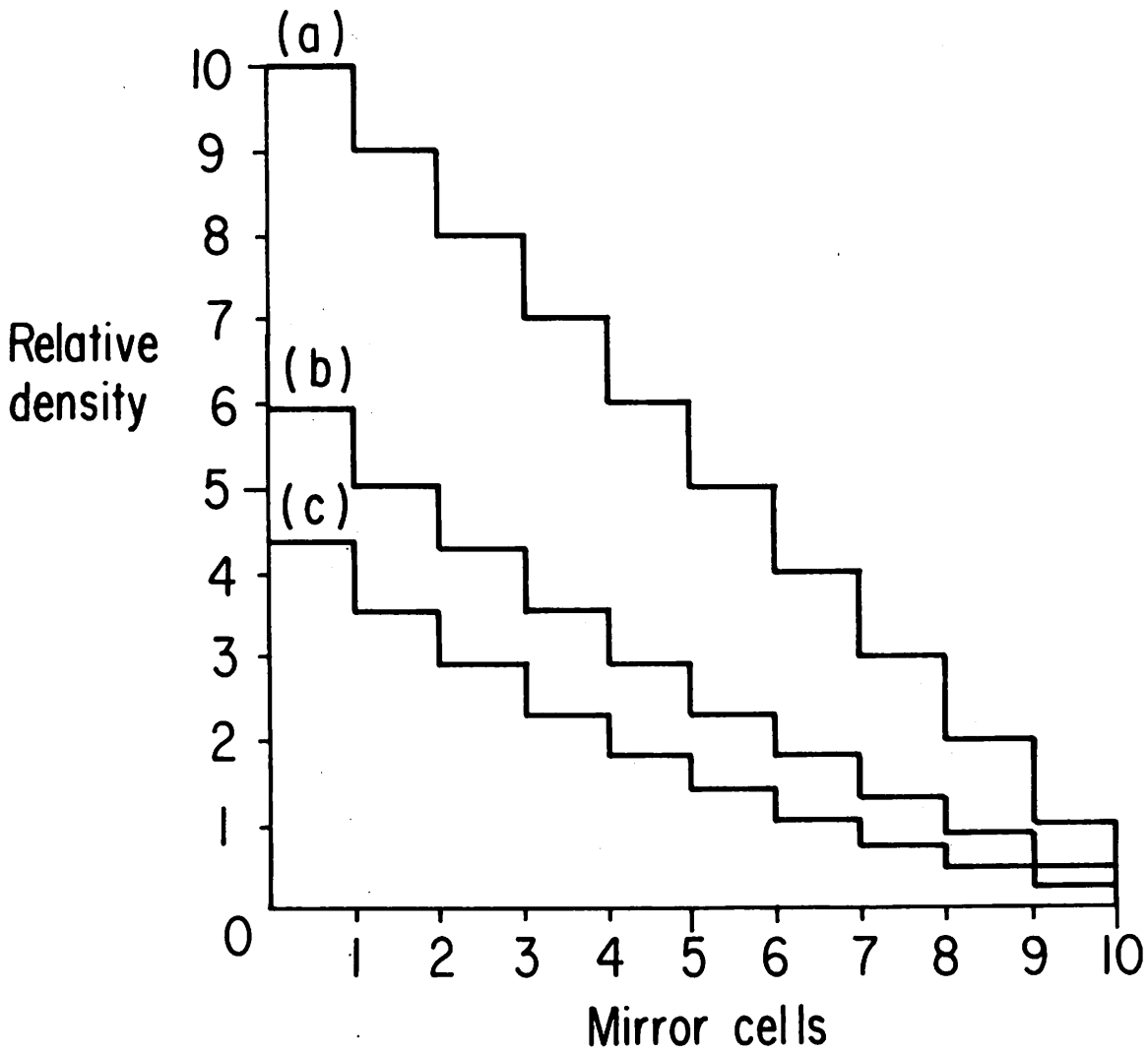


Fig. C1 Theoretical discrete multiple-mirror density profiles in the presence of radial loss: (a) No radial loss; (b) Radial loss equal to axial loss; (c) radial loss twice axial loss.

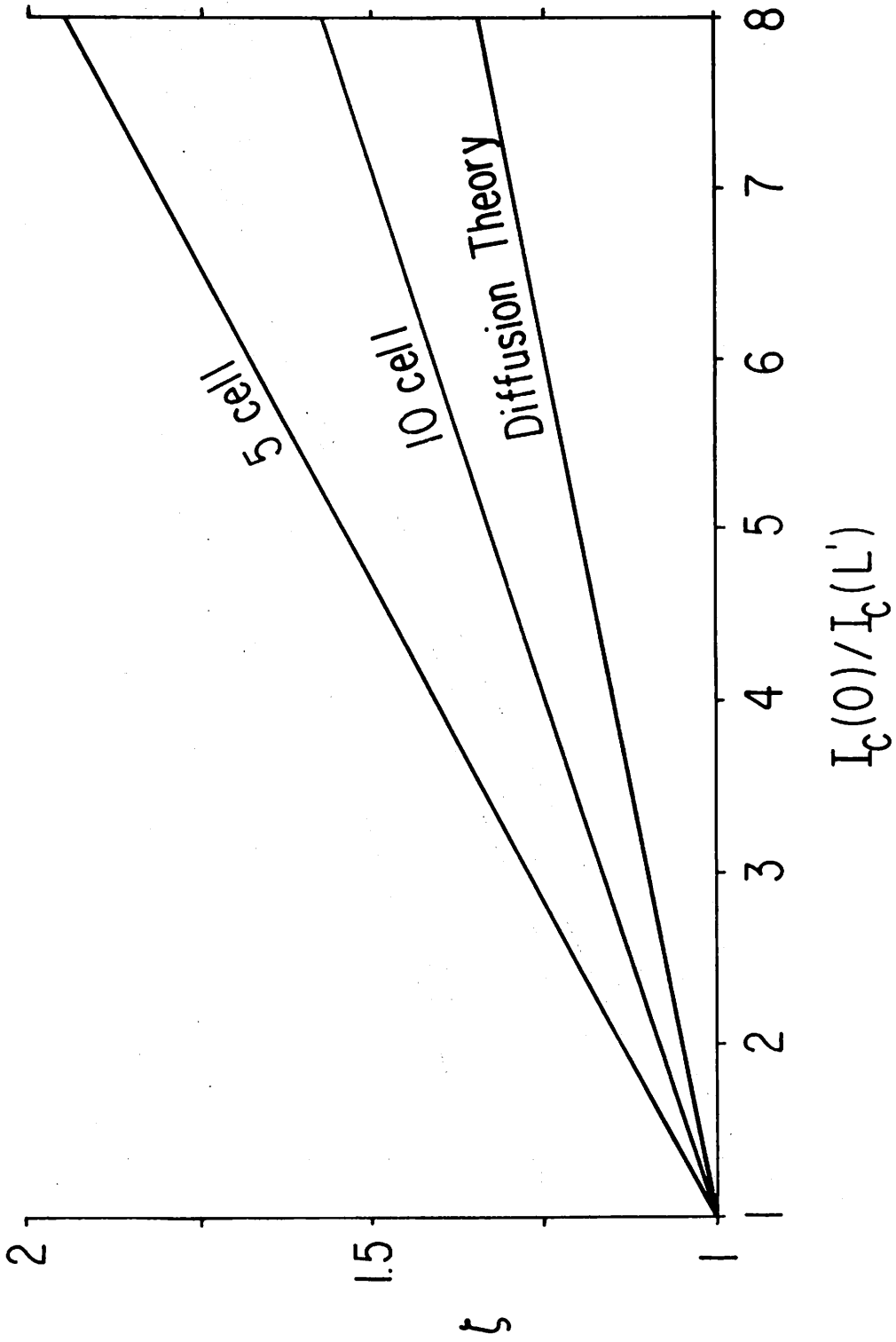


Fig. C2 Theoretical correction factors ζ as a function of radial loss associated collector

current drop ratio $I_c(0)/I_c(L')$, for a discrete 5 and 10 cells system, and a continuous diffusive system.